Orographic Effects on Landfalling Lake-Effect Systems

THOMAS M. GOWAN,[a] W. JAMES STEENBURGH,[a] AND JUSTIN R. MINDER[b]

[a] *Department of Atmospheric Sciences, University of Utah, Salt Lake City, Utah*
[b] *Department of Atmospheric and Environmental Sciences, University at Albany, State University of New York, Albany, New York*

(Manuscript received 28 November 2021, in final form 1 May 2022)

ABSTRACT: Landfalling lake- and sea-effect (hereafter lake-effect) systems often interact with orography, altering the distribution and intensity of precipitation, which frequently falls as snow. In this study, we examine the influence of orography on two modes of lake-effect systems: long-lake-axis-parallel (LLAP) bands and broad-coverage, open-cell convection. Specifically, we generate idealized large-eddy simulations of a LLAP band produced by an oval lake and broad-coverage, open-cell convection produced by an open lake (i.e., without flanking shorelines) with a downstream coastal plain, 500-m peak, and 2000-m ridge. Without terrain, the LLAP band intersects a coastal baroclinic zone over which ascent and hydrometeor mass growth are maximized, with transport and fallout producing an inland precipitation maximum. The 500-m peak does not significantly alter this structure, but slightly enhances precipitation due to orographic ascent, increased hydrometeor mass growth, and reduced subcloud sublimation. In contrast, a 2000-m ridge disrupts the band by blocking the continental flow that flanks the coastlines. This, combined with differential surface heating between the lake and land, leads to low-level flow reversal, shifting the coastal baroclinic zone and precipitation maximum offshore. In contrast, the flow moves over the terrain in open lake, open-cell simulations. Over the 500-m peak, this yields an increase in the frequency of weaker (<1 m s^{-1}) updrafts and weak precipitation enhancement, although stronger updrafts decline. Over the 2000-m ridge, however, buoyancy and convective vigor increase dramatically, contributing to an eightfold increase in precipitation. Overall, these results highlight differences in the influence of orography on two common lake-effect modes.

SIGNIFICANCE STATEMENT: Landfalling lake- and sea-effect snowstorms frequently interact with hills, mountains, and upland regions, altering the distribution and intensity of snowfall. Using high-resolution numerical modeling with simplified lake shapes and terrain features, we illustrate how terrain features affect two common types of lake-effect storms and why long-lake-axis-parallel (LLAP) bands can feature high precipitation rates but weaker orographic enhancement than broad-coverage, open-cell convection.

KEYWORDS: Boundary layer; Snow; Precipitation; Mesoscale processes; Orographic effects; Clouds; Large eddy simulations

1. Introduction

Cold-air outbreaks over relatively warm bodies of water can lead to lake- or sea-effect (hereafter lake-effect) systems that often interact with downstream orography, modifying the distribution and intensity of precipitation that often falls as snow. For example, the Tug Hill Plateau (hereafter Tug Hill) downstream of Lake Ontario and mountains of the Japanese islands of Honshu and Hokkaido near the Sea of Japan (also known as the East Sea) are well known for prolific lake-effect snowfall (e.g., Veals et al. 2018, 2019; Steenburgh and Nakai 2020). Over Tug Hill, which gradually rises ~500 m just east of Lake Ontario, a pronounced climatological snowfall maximum exists with average annual snowfall exceeding 450 cm (Hartnett et al. 2014; Veals and Steenburgh 2015). In the mountains of Honshu and Hokkaido near the Sea of Japan, which in some areas reach over 2000 m MSL, annual snowfall can exceed 1300 cm, with seasonal snow depths reaching 7 m or more (Yamaguchi et al. 2011; Steenburgh and Nakai 2020). In both regions, snowfall rates in individual storms can exceed 10 cm h^{-1} (Kawamoto et al. 1963; Burt 2007; Kristovich et al. 2017).

The mode of lake-effect precipitation depends on factors such as environmental conditions, shoreline geometry, and orography (Braham and Kelly 1982; Braham 1983, 1986; Hjelmfelt 1990; Niziol et al. 1995; Laird et al. 2003a,b; Nakai et al. 2005). Broadly, these modes can be divided into two categories: those produced by boundary layer circulations and those produced by thermally forced or terrain-driven circulations. Lake-effect precipitation generated by boundary layer circulations often exhibits broad-area coverage and can take the form of open cells during weak vertically sheared flows (Atkinson and Zhang 1996) or longitudinal (L-mode) or transversal (T-mode) bands during strong vertically sheared flows (Tsuchiya and Fujita 1967; Nakai et al. 2005). L-mode bands orient parallel to the mean flow, whereas T-mode bands orient perpendicular to the mean flow. Lake-effect precipitation generated by thermally forced or terrain-driven circulations can feature a single, mesoscale band of heavy precipitation. Over elongated lakes, such as Lake Ontario, land-breeze convergence often produces a long-lake-axis-parallel (LLAP) band (Peace and Sykes 1966; Reinking et al. 1993; Steiger et al. 2013; Steenburgh and Campbell 2017). Similar thermally forced bands can also form over bays and channels (e.g., Norris et al. 2013; Mazon et al. 2015). Over the Sea of Japan, thermally and terrain-forced convergence

Corresponding author: Thomas M. Gowan, tom.gowan@gmail.com

DOI: 10.1175/MWR-D-21-0314.1

downstream of the Korean Highlands occasionally produces a mesoscale band of heavy precipitation, known as the Japan Sea polar airmass convergence zone (JPCZ; Nagata 1987, 1991; Nagata et al. 1986; Ohigashi and Tsuboki 2007; West et al. 2019).

Gowan et al. (2021, hereafter G21) recently investigated and compared the downstream evolution and coastal-to-inland transition of a LLAP band with broad-coverage, open-cell convection using idealized large-eddy simulations without orography. The LLAP band featured thermally forced land-breeze convergence over the mid-lake axis and a secondary, diabatically enhanced, cross-band circulation that produced a mesoscale band of heavy precipitation. A cold pool formed downstream of the lake due to flanking airstreams that avoided lake modification and sublimational cooling beneath the band. At the interface of the cold pool and the lake-modified air, a coastal baroclinic zone formed. Here, ascent and hydrometeor mass growth occurred, with hydrometeor transport and fallout producing a precipitation maximum inland from the coast. In contrast, the broad-coverage, open-cell convection produced widespread, light accumulations. Over the lake, the open cells grew larger and deeper as they progressed downstream before undergoing a convective-to-stratiform transition near and inland from the downstream coastline. The transition featured a decay in convective vigor, the development of widespread mesoscale ascent, and increased hydrometeor mass growth, which contributed to an inland precipitation maximum.

In this study, we build upon G21 by adding downstream orography to simulations of the two lake-effect systems. In general, the influence orography has on precipitation is determined by several factors including the shape and size of the terrain, the large-scale storm environment, the speed and stability of the incident flow, and the microphysical time scale (Roe 2005; Smith 2006; Houze 2012). Prior studies of orographic influences on lake-effect precipitation have illustrated the importance of the height of the terrain, strength of the incident flow, magnitude of the lake-induced convective available potential energy (LCAPE), and the mode of the lake-effect system (Campbell et al. 2016; Veals et al. 2018, 2019, 2020). Over Tug Hill, banded (i.e., LLAP band) lake-effect periods often feature higher precipitation rates, but weaker orographic enhancement, than non-banded (i.e., broad-coverage) periods. Mechanisms contributing to the Tug Hill precipitation maximum include the orographic suppression of subcloud sublimation (Minder et al. 2015; Campbell and Steenburgh 2017), ascent associated with land-breeze convergence (Bergmaier et al. 2017; Campbell and Steenburgh 2017), and a convective-to-stratiform transition (Minder et al. 2015; Gowan et al. 2021). The latter two are non-orographic effects evident in simulations without orography (Campbell and Steenburgh 2017; Gowan et al. 2021). Although profiling radar statistics indicate that the depth and intensity of lake-effect convection does not commonly increase over Tug Hill (Minder et al. 2015), some conceptual models depict this behavior over inland orography (e.g., Lackmann 2011, see his Fig. 9.21).

In contrast to the relatively modest Tug Hill, lake-effect systems over the Sea of Japan encounter formidable mountain ranges along the west coast of Japan, sometimes leading to flow blocking. Lake-effect periods with blocking feature upstream convergence, sometimes enhanced by katabatic flows (i.e., land breezes), resulting in the heaviest precipitation falling over the upstream lowlands or the Sea of Japan (Ishihara et al. 1989; Ohigashi et al. 2014; Kusunoki et al. 2004; Veals et al. 2019, 2020). During unblocked periods, mechanisms proposed to contribute to orographic enhancement include the suppression of subcloud sublimation (Murakami et al. 1994), seeder–feeder (Saito et al. 1996; Murakami et al. 1994) and invigoration of convection (Nakai et al. 1990; Saito et al. 1996).

In this paper we investigate and compare the interactions of a LLAP band and broad-coverage, open-cell convection with downstream orography by adding a downstream 500-m bell-shaped peak and a 2000-m ridge to the idealized large-eddy simulations presented in G21. In total, we analyze six simulations based on two simplified lake shapes (oval and open), which generate a LLAP band and open-cell convection, respectively, and three terrain configurations (coastal plain, 500-m peak, and 2000-m ridge). This enables an intercomparison of the orographic effects across a portion of the spectrum of lake-effect modes and terrain shapes and sizes and allows us to illustrate why banded (i.e., LLAP band) lake-effect periods often feature higher precipitation rates, but weaker orographic enhancement than non-banded (i.e., broad-coverage) periods.

The next section describes the design, configuration, and initial conditions of the numerical simulations. Sections 3 and 4 identify and examine the orographic effects and mechanisms in LLAP band and broad coverage, open-cell lake-effect simulations, respectively. A summary and conclusions, including a discussion of significance of these findings for understanding the interaction of lake-effect and similar shallow cumuliform precipitation systems with downstream orography, are provided in section 5.

2. Data and methods

a. *Model configuration*

Simulations were generated using Cloud Model 1 version 19 (CM1; Bryan and Fritsch 2002) with model configurations identical to those described in G21 except for the addition of downstream topography and a slight modification to the lateral boundary conditions discussed below. We conducted and analyzed six simulations resulting from all unique combinations of two lake shapes (oval or open) and three terrain features [a coastal plain (i.e., no terrain), 500-m bell-shaped peak, or 2000-m ridge]. All simulations feature a domain size of 562.5 km × 125 km × 8 km (x-, y-, and z- dimensions, respectively), with a uniform horizontal grid spacing of 125 m and a vertical grid spacing of 100 m up to 4 km, above which the grid spacing is smoothly stretched to 500 m. The physics parameterization suite includes the Smagorinsky (1963) turbulence, Thompson et al. (2008) cloud microphysics, revised

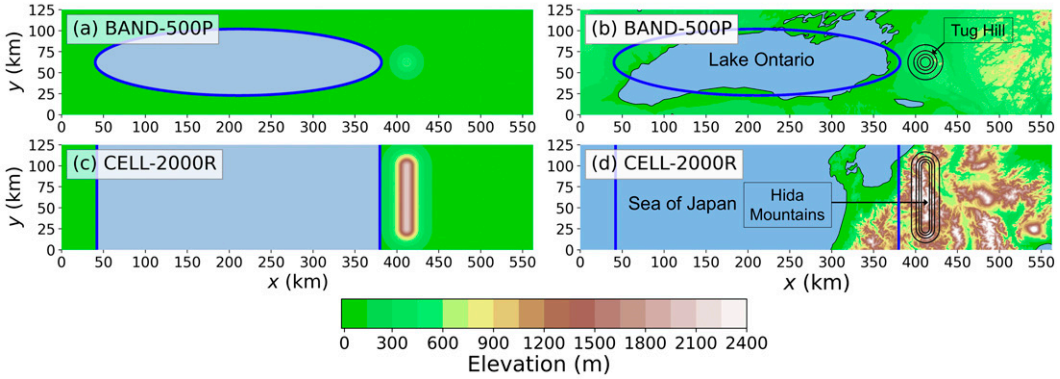

FIG. 1. (a) Oval lake and 500-m peak CM1 domain used for BAND-500P [elevation (m MSL) shaded following scale at bottom]. (b) Lake Ontario–Tug Hill region [lake in blue and elevation (m MSL) shaded following scale at bottom] with idealized oval lake (blue line) and black contours representing 500-m peak terrain (contoured every 100 m from 100 to 400 m) from BAND-500P. (c) As in (a), but for open lake and 2000-m ridge CM1 domain used for CELL-2000R. (d) As in (b), but for Sea of Japan–Hida Mountains region and black contours are every 400 m from 400 to 1600 m.

MM5 surface layer (Jiménez et al. 2012), and five-layer thermal diffusion land surface (Dudhia 1996) schemes. As described in greater detail by G21, shortwave and longwave radiation were not included to help maintain steady surface and land surface temperatures, the Coriolis force was omitted because it had a negligible impact during testing, and lake-surface temperatures were fixed. Land-use characteristics were based on the U.S. Geological Survey (USGS) winter "mixed forest" category with soil moisture turned off, resulting in the lake being the only source of moisture.

Following G21, Rayleigh damping layers were used in all simulations to reduce spurious gravity wave reflections. We applied a 2-km Rayleigh damping layer to the upper boundary and 10-km-wide Rayleigh damping layers to the inflow and outflow (parallel to y axis) boundaries. At the inflow, Rayleigh damping also acts to maintain the base-state wind profile. In all simulations, boundary conditions are open radiative at the inflow and outflow lateral boundaries, semislip at the bottom boundary [described in Markowski and Bryan (2016)], and free slip at the upper boundary. As discussed in G21, the flow-parallel (parallel to x axis) lateral boundary conditions are open radiative in simulations with an oval lake and periodic in simulations with an open lake. Open-radiative lateral boundary conditions must be used with an oval lake because land breezes form and generate opposing flows on either side of the long-lake axis. We slightly modify the open-radiative boundary conditions used in G21 by restricting the domain-wide outward mass flux so that it does not exceed the inward mass flux. This restriction helps to maintain cross-flow symmetry in runs with topography but does not meaningfully change the simulations.

b. Lake and terrain geometries

The geometries of the oval and open lake are identical to those described in G21. We designed the oval lake to be an idealized representation of Lake Ontario and other elongated bodies of water (cf. Figs. 1a,b) and the open lake to be an idealized representation of the Sea of Japan or other large bodies of water where there are no nearby coastlines flanking the flow (cf. Figs. 1c,d). These idealized lakes notably lack coastal irregularities that can affect snowband initiation and evolution (e.g., Atlas et al. 1983; Andersson and Gustafsson 1994; Tripoli 2005; Mazon et al. 2015; Steenburgh and Campbell 2017).

The terrain configurations include a 500-m bell-shaped peak and a 2000-m ridge. These idealized configurations are meant to provide insights into some of the processes that occur where lake-effect systems interact with lower terrain features such as near the Laurentian Great Lakes (e.g., Minder et al. 2015; Campbell and Steenburgh 2017; Veals et al. 2018) and North Sea (Norris et al. 2013) and larger mountain barriers such as near the Sea of Japan (Veals et al. 2019; Steenburgh and Nakai 2020), Lake Constance (Umek and Gohm 2016), Great Salt Lake (Steenburgh et al. 2000; Alcott and Steenburgh 2013), Black Sea (Kindap 2010; Markowski and Richardson 2010), and Caspian Sea (Nicholls and Toumi 2014). Specifically, these idealized representations are intended to approximate the Tug Hill near Lake Ontario and the Hida Mountains of Japan (Fig. 1). Both terrain features are centered at $x = 411.75$ km, $y = 62.5$ km. Following Dörnbrack et al. (2005), the topography of the 500-m bell-shaped peak is given by

$$h(x, y) = h_m \left[1 + \left(\frac{\sqrt{x^2 + y^2}}{a} \right)^2 \right]^{-3/2}, \quad (1)$$

where h_m is the maximum height (500 m), a is the half-width (15 km), and the origin is at $x = 411.75$ km and $y = 62.5$ km. One difference between this idealization and the real Tug Hill is the latter has a broader profile with a flat top. To construct the 2000-m ridge, we modify Eq. (1), resulting in

$$h(x,y)=\begin{cases} h_m\left[1+\left(\dfrac{x}{a}\right)^2\right]^{-3/2}, & |y-y_c|\le b \\ h_m\left(1+\left\{\dfrac{\sqrt{x^2+\left[y-\mathrm{sgn}(y-y_c)(y_c+b)\right]^2}}{a}\right\}^2\right)^{-3/2}, & |y-y_c|>b, \end{cases} \tag{2}$$

where $h_m = 2000$ m, $a = 12$ km, y_c is the distance to the center of the domain in the y direction (62.5 km), and b is the half-length (37.5 km), and the origin is at $x = 411.75$ km, $y = 62.5$ km. We follow the same naming convention used in G21 in which we refer to oval-lake simulations as BAND because they produce a LLAP band and open-lake simulations as CELL because they produce open-cell convection. We then append the terrain type [CTL ("control") for no terrain, 500P for 500-m peak, and 2000R for 2000-m ridge] to BAND and CELL (Table 1).

c. Environmental conditions

All simulations were initialized with the same environmental conditions, which are identical to those used in G21. The thermodynamic profile is an idealization of a typical lake-effect profile based on the visual inspection of observed soundings upstream of the Great Lakes and Sea of Japan during strong lake-effect events and features a well-mixed layer from the surface to 1.9 km, a capping inversion from 1.9 to 2.1 km, and a stable air mass above 2.1 km (Fig. 2). The lake-surface temperature was set to a constant 8.35°C, which is near average for Lake Ontario in mid-November (Great Lakes Environmental Research Laboratory 2021) and close to the mean sea surface temperature midway between the Asian mainland and central Honshu coasts of the Sea of Japan in February (see Fig. 3b of Steenburgh and Nakai 2020). We initialized the land surface with a temperature of −5.15°C, close to the temperature of the lowest level in the sounding (−6.15°C). The initial 850-hPa temperature is −18.4°C, resulting in a lake–850-hPa temperature difference of 26.75°C, which studies suggest can result in heavy lake-effect precipitation (Niziol 1987; Niziol et al. 1995; Veals et al. 2018). Winds were initialized with a horizontally and vertically uniform u-component velocity of 12.5 m s^{-1}, which falls between the 60th and 80th percentile of mean 950–850-hPa wind speeds during lake-effect events over Lake Ontario (Veals et al. 2018). We also included random, domain-wide 0.1 K potential-temperature perturbations in the initial conditions to seed turbulence.

As in G21, we focus primarily on hours 9–13 when the simulations exhibit a quasi–steady state. During this period, the lake-effect systems are fully developed, and hourly means vary by less than 20%. In the analyses, most variables are averaged over this 4-h period. For brevity and convenience, we opt to remove the "time-mean" modifier preceding variable names. Thus, unless stated otherwise, all variables are averaged over this 4-h period. Details regarding temporal and spatial averaging are provided in figure captions.

3. BAND orographic effects

a. Precipitation distribution

We begin by examining how downstream terrain modifies a LLAP band by comparing the oval-lake control simulation without orography (BAND-CTL) to simulations with a 500-m peak (BAND-500P) and 2000-m ridge (BAND-2000R; Fig. 3). To facilitate this comparison, Fig. 3 includes the average and maximum precipitation rates for the plotted region and the orographic ratio, OR, defined as the ratio of area-averaged precipitation within the region encompassing the highest terrain in BAND-500P (>250 m) or BAND-2000R (>1000 m) to that in the corresponding region of BAND-CTL (regions identified by solid yellow lines in Figs. 3d,e). For BAND-2000R we also compute $\mathrm{OR}_{\mathrm{band}}$, the orographic ratio in the area encapsulating the BAND-CTL precipitation band (dashed yellow lines in Fig. 3e).

Comparing BAND-500P to BAND-CTL shows that a 500-m peak has minimal impact on the lake-effect band (Figs. 3a,b). Both simulations generate over-lake convergence with heavy precipitation near the mid-lake axis that extends inland from the downstream coast, coastal baroclinity, and a cold pool downstream of the lake. Total area-averaged precipitation rates increase slightly from BAND-CTL to BAND-500P (0.25–0.27 mm h^{-1}), as do maximum precipitation rates (5.00–5.77 mm h^{-1}). The location of the maximum is shifted ~5 km upstream in BAND-500P, where it is located over the windward slope of the peak (not explicitly shown). Inland penetration of the band is weaker in BAND-500P, which also features a narrower downstream cold pool.

Differencing the precipitation distributions reveals that BAND-500P exhibits a slight lateral displacement in band position over the lake relative to BAND-CTL (Fig. 3d). We attribute this to the use of random initial temperature perturbations and open-radiative x-axis lateral boundary conditions, which make it difficult to maintain perfect symmetry. Near and over the 500-m peak, the BAND-500P precipitation band is broader, which is reflected in increased precipitation on the windward and flanking sides of the peak. In the lee, the band decays more rapidly with inland extent with less precipitation in a narrow strip that extends downstream from directly over the peak. Overall, the OR is 1.13, indicating a 13% increase in area-average precipitation over the 500-m peak. This increase is less than the ~30% increase Campbell and Steenburgh (2017; see their Fig. 4) found in real-data simulations of a LLAP band with and without Tug Hill. The orographic influences on the precipitation distribution are, however, remarkably similar, including broadening of the band, increased windward-slope precipitation, and decreased leeward precipitation.

TABLE 1. Lake and topography configuration for each simulation.

Name	Lake	Topography
BAND-CTL	Oval	None
BAND-500P	Oval	500-m peak
BAND-2000R	Oval	2000-m ridge
CELL-CTL	Open	None
CELL-500P	Open	500-m peak
CELL-2000R	Open	2000-m ridge

In contrast, the lake-effect band is strongly modified in BAND-2000R. Over the lake, upstream of x = 360 km, BAND-CTL and BAND-2000R feature similar precipitation distributions and lowest-level wind and potential temperature patterns (cf. Figs. 3a,c). Near x = 360 km, the band in BAND-2000R intersects the coastal baroclinic zone, which is farther offshore and exhibits greater cross-band extent than in BAND-CTL. Precipitation maximizes over the coastal baroclinic zone and declines inland over the coastal lowlands and windward slope of the ridge; however, the precipitation area and cold pool coverage are broader. Overall, the total area-average and maximum precipitation rates are ~35% and ~45% greater, respectively, in BAND-2000R, but the precipitation maximum is shifted upstream with the coastal baroclinic zone. Over the ridge, precipitation is more widespread in BAND-2000R, but weaker. An OR of 1.01 indicates that the total precipitation mass over the upper-elevations of the ridge is nearly identical to the corresponding region in BAND-CTL, but an OR_{band} of 0.58 reflects a decrease in precipitation where the band extends inland in BAND-CTL (see also Fig. 3e). Thus, the presence of the 2000-m ridge strongly alters the band structure, shifting the precipitation maximum upstream over the lake and broadening the band as it moves inland, resulting in widespread light precipitation over the ridge and decreased inland penetration.

Close-ups over the downstream coastline better highlight how the LLAP band is modified by a 500-m peak and 2000-m ridge (Fig. 4). Overall, the coastal-to-inland transition in BAND-500P is similar to BAND-CTL (Figs. 4a–d). Both simulations feature a maximum in 1–1.5 km AGL vertically averaged vertical velocity and a weakening of precipitation rates where the band intersects the coastal baroclinic zone at the downstream coastline. Farther inland, ascent weakens, the band broadens, and precipitation rates maximize. However, precipitation in BAND-2000R maximizes along the coastal baroclinic zone, which is farther offshore, near x = 365 km, due to low-level flow reversal and associated offshore flow (Figs. 4e,f). Along the coastal baroclinic zone, low-level convergence between the incident flow over the lake and the offshore flow generates a region of strong ascent across the entire y-extent of the lake resulting in a broad region of precipitation. In contrast to BAND-CTL and BAND-500P, which produce a broadening of the band and a precipitation maximum inland from the coastal baroclinic zone, precipitation decreases rapidly with inland extent in BAND-2000R, with spillover confined to the immediate lee of the ridge (cf. Figs. 4a,c,e; see also Fig. 3c for spillover).

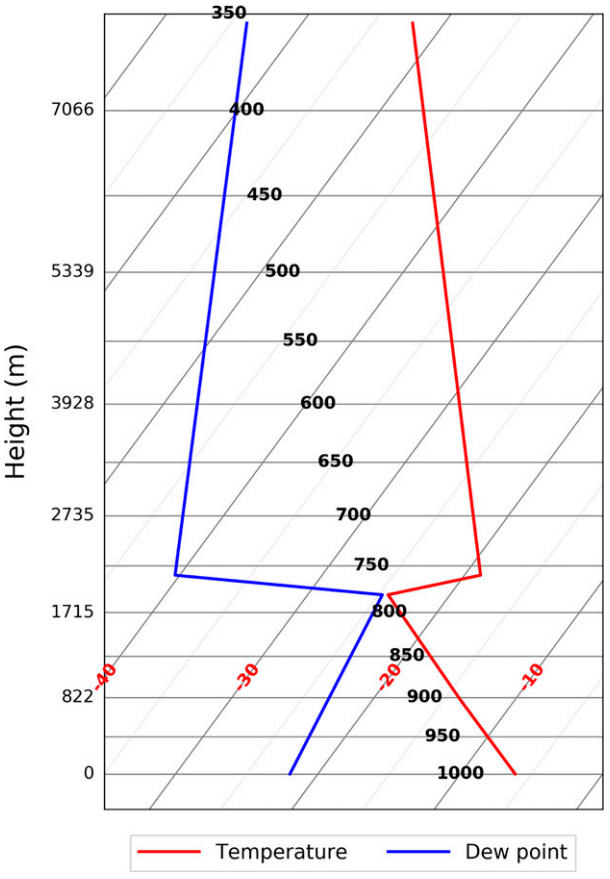

FIG. 2. Skew T–log$p$ diagram illustrating the thermodynamic profile used to initialize all simulations.

b. *Vertical structure and hydrometeor tendencies*

We now examine the vertical structure of hydrometeor mass and tendencies, which helps explain the precipitation distribution in each simulation. Following G21, we use along-band cross sections of total hydrometeor mixing ratio, $\overline{q}$, and total hydrometeor mixing ratio tendency due to phase changes, $\overline{\text{qten}}$, although we average over the middle 20 km of the band (i.e., y = 52.5–72.5 km, Fig. 5) rather than the middle 10 km as in G21. $\overline{q}$ is given by

$$\overline{q} = \overline{q}_c + \overline{q}_r + \overline{q}_i + \overline{q}_g + \overline{q}_s, \tag{3}$$

where $\overline{q}_c$, $\overline{q}_r$, $\overline{q}_i$, $\overline{q}_g$, and $\overline{q}_s$ are the cloud water, rain, ice, graupel, and snow mixing ratios, respectively. The overbar here and elsewhere denotes time means during the steady-state period. Although we account for all hydrometeor species computed by the Thompson et al. (2008) cloud microphysics scheme, $\overline{q}$ is composed primarily of $\overline{q}_s$ in all BAND simulations (~98% in the cross sections in Fig. 5).[1]

[1] G21 reported a lower percentage (96.2%) for BAND-CTL. The difference is due to G21 averaging over 10 km instead of 20 km.

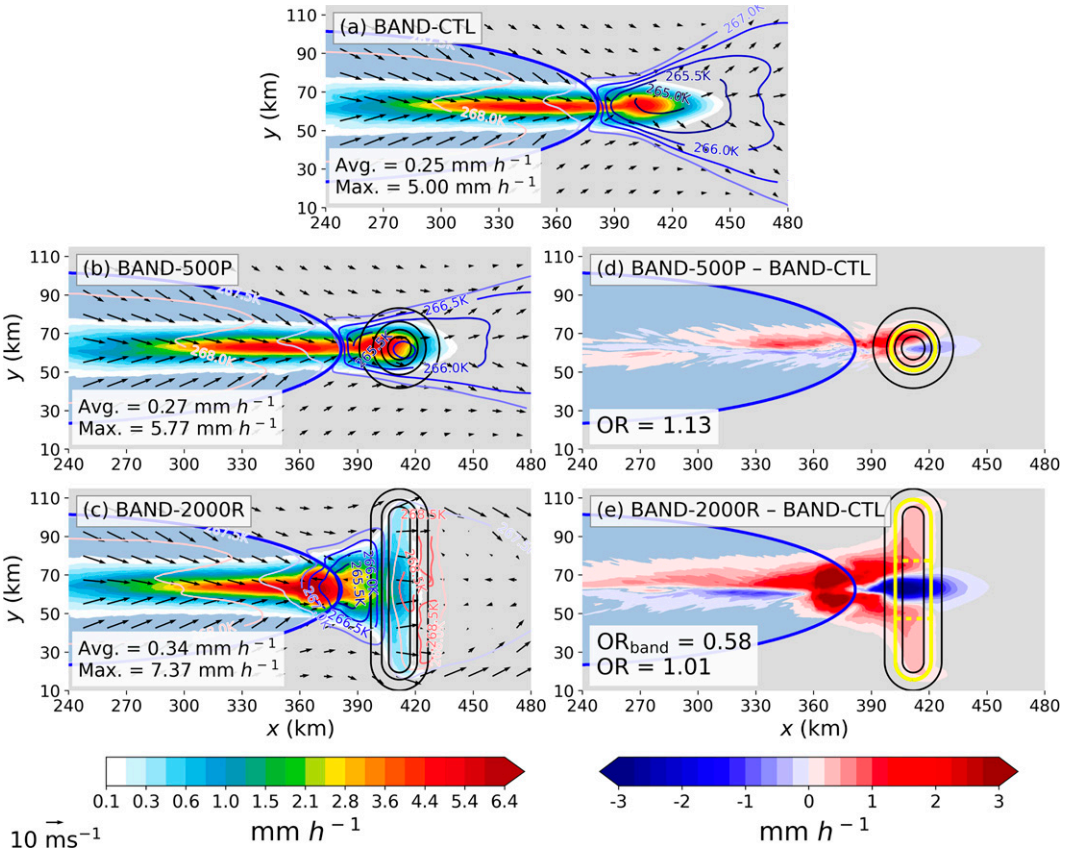

FIG. 3. (a) BAND-CTL 4-h time-mean precipitation rate (mm h^{-1}, scale at bottom left), lowest-level (50-m) wind vectors (scale at bottom left), and lowest-level potential temperature (blue to red contours every 0.5 K) with inset area-average and maximum (over entire area of subplot) 4-h time-mean precipitation rate annotated. Potential temperature smoothed with a 40 × 40 point uniform filter. (b),(c) As in (a), but for BAND-500P and BAND-2000R, respectively. (d) BAND-500P − BAND-CTL 4-h time-mean precipitation rate (mm h^{-1}, scale at bottom right) with inset orographic ratio (OR) computed over region enclosed by yellow solid line. (e) As in (d), but for BAND-2000R − BAND-CTL and with inset orographic ratio for band location (OR_{band}) computed over region enclosed by yellow dashed line. Thick blue line is coastline and black contours are elevations every 100 m from 100 to 400 m in (b) and (d) and every 500 m from 500 to 1500 m in (c) and (e).

Consistent with the previous sections, there are only small differences in the vertical structure and hydrometeor mass distribution in BAND-CTL and BAND-500P over the lake (Figs. 5a,b). Both simulations feature a zone of high $\overline{q}$ (>1 g kg^{-1}) from $z \simeq$ 1–2 km that strengthens with downstream extent and maximizes at ~1.4 g kg^{-1} over the coastal baroclinic zone. Farther downstream, ascent weakens and the zone of high $\overline{q}$ arcs down and meets the surface from x = 400–410 km, intersecting the coastal plain in BAND-CTL and windward slope of the peak in BAND-500P. This pattern reflects hydrometeor mass growth and lofting over the coastal baroclinic zone and subsequent downstream transport and fallout, as described in greater depth by G21. The inland precipitation maximum is collocated with the intersection of high $\overline{q}$ with the surface in each simulation.

A careful comparison shows higher low-level $\overline{q}$ values over the windward slope of the peak in BAND-500P compared to similar locations in BAND-CTL. At the surface, $\overline{q}$ maximizes at ~0.85 g kg^{-1} in BAND-500P but only ~0.7 g kg^{-1} in BAND-CTL. Overall, these $\overline{q}$ distributions are consistent with a broader, more intense precipitation maximum in BAND-500P due to the influence of the 500-m peak.

To explain these differences between BAND-CTL and BAND-500P, we focus on $\overline{\text{qten}}$, which indicates hydrometeor mass growth where positive and hydrometeor mass loss where negative (Figs. 5d,e). The latter reflects sublimation below cloud base, which is located at the transition from negative to positive $\overline{\text{qten}}$ values at $z \simeq$ 0.5–1.0 km. Just downstream of the lake, above the coastal baroclinic zone (at $z \simeq$ 1.5 km), both simulations feature a maximum in hydrometeor mass growth ($\overline{\text{qten}} > 4 \times 10^{-4}$ g kg^{-1} s^{-1}) and ascent ($\overline{w} \simeq 0.7$ m s^{-1}). Farther downstream, along the arcing path of greatest $\overline{q}$ (Figs. 5a,b), BAND-CTL features a relatively deep (~1 km) region of substantial low-level hydrometeor mass loss, whereas BAND-500P features a zone of weak hydrometeor mass growth that extends downward nearly to the surface of the peak. Thus, while sublimation results in low-level hydrometeor loss in BAND-CTL, orographic ascent and the decreased distance between the surface and cloud base results in increased

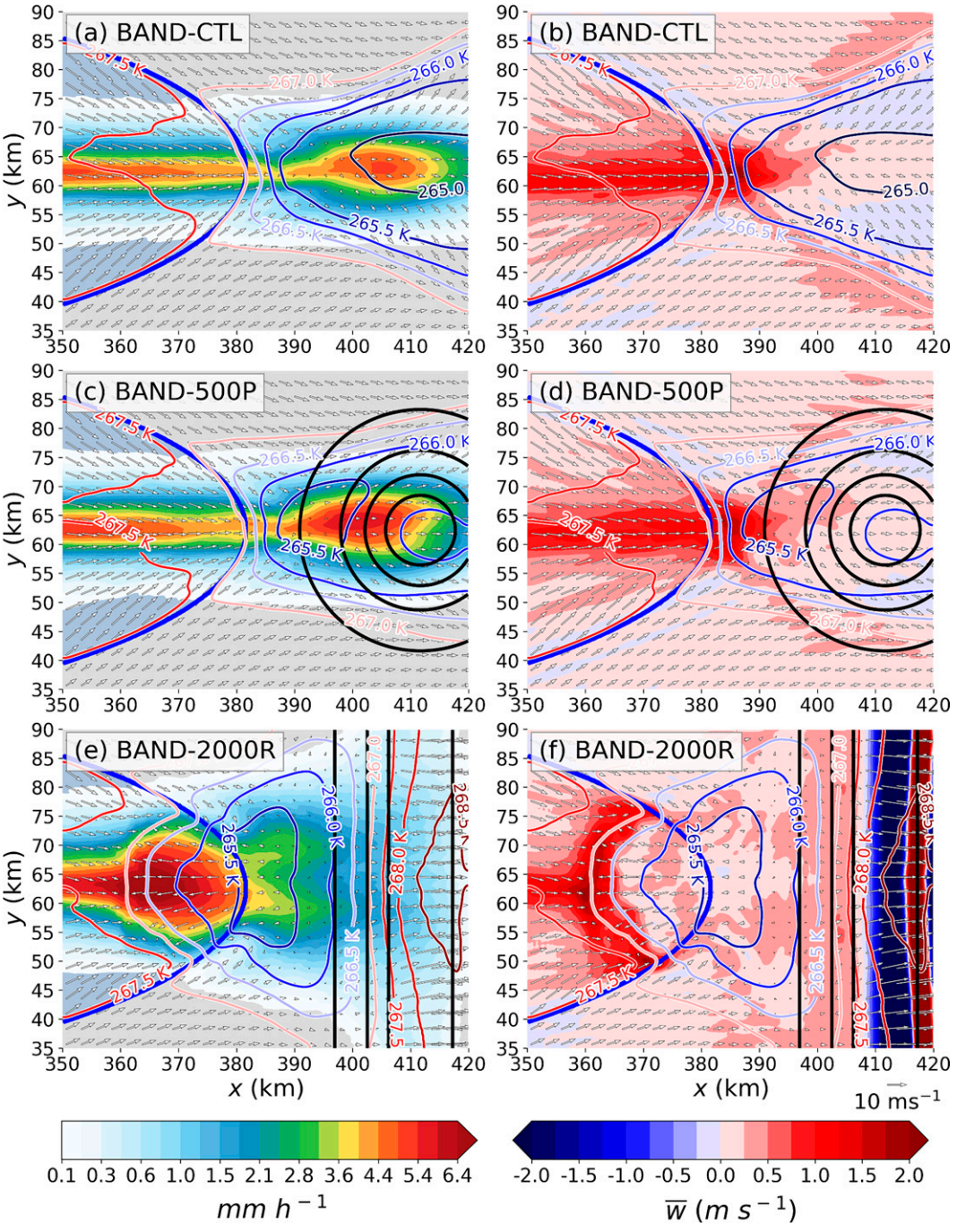

FIG. 4. (a) BAND-CTL 4-h time-mean precipitation rate (mm h^{-1}, scale at bottom left), lowest-level (50-m) wind vectors (scale at bottom right), and lowest-level potential temperature (blue to red contours every 0.5 K). Thick blue line represents lake outline. (b) As in (a), but color fill is 4-h time-mean, 1–1.5 km AGL vertically averaged vertical velocity ($\overline{w}$; m s^{-1}, scale at bottom right). (c),(d) As in (a) and (b), but for BAND-500P with black elevation contours every 100 m from 100 to 400 m. (e),(f) As in (a) and (b), but for BAND-2000R with black elevation contours every 500 m from 500 to 1500 m. Potential temperature and $\overline{w}$ smoothed with a 20 × 20 and 10 × 10 point uniform filter, respectively.

hydrometeor mass growth and reduced subcloud sublimation in BAND-500P, yielding a broader, stronger precipitation maximum. This finding is qualitatively similar to Campbell and Steenburgh (2017), who show that Tug Hill increased hydrometeor growth and reduced sublimational losses in simulations of Ontario Winter Lake-effect Systems (OWLeS) IOP2b. Minder et al. (2015) also reported evidence from profiling radar observations of lake-effect storms of a reduction

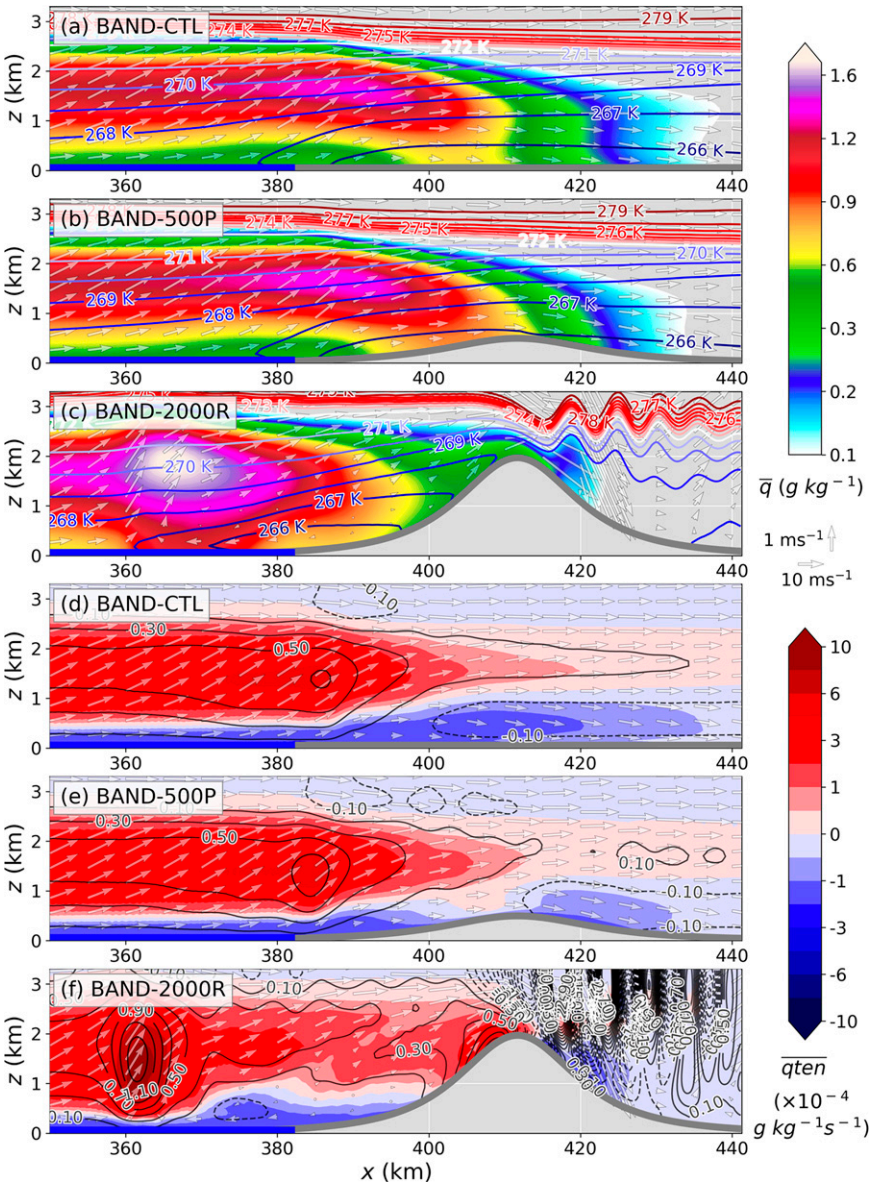

FIG. 5. (a) BAND-CTL x–z cross section of 4-h time-mean, 20-km y-averaged (over the middle of band) total hydrometeor mixing ratio ($\overline{q}$; g kg^{-1}, scale on upper right), cross-section-parallel wind vectors (scale at middle right), and potential temperature (blue to red contours every 1 K). Thick blue line represents lake surface. (b),(c) As in (a), but for BAND-500P and BAND-2000R, respectively. (d),(e) As in (a)–(c), but with total hydrometeor mass tendency ($\overline{qten}$; ×10^{-4} g kg^{-1} s^{-1}, scale on lower right) and vertical velocity (black contours every 0.2 m s^{-1} with zero not plotted and negative contours dashed). Vertical velocity smoothed with a 20 × 20 point uniform filter.

in sublimational losses from the Lake Ontario coastal plain to Tug Hill.

In contrast, cross sections of BAND-2000R feature an offshore coastal baroclinic zone ~20 km farther upstream than in BAND-CTL and BAND-500P where the incident flow meets offshore flow that develops just inland from the coast and accelerates over the lake (Figs. 5c,f). Convergence between these airstreams leads to strong ascent (>1.3 m s^{-1}), intense hydrometer mass growth, and a $\overline{q}$ maximum > 1.6 g kg^{-1}, larger than found over and downstream of the coastal baroclinic zone in BAND-CTL and BAND-500P. Instead of a downstream-arcing region of high $\overline{q}$ to the surface, the region of high $\overline{q}$ in BAND-2000R is oriented nearly vertical and intersects the surface after falling through the cold, offshore, low-level flow. This yields a precipitation maximum on the cold side of the surface convergence zone. The relative lack of horizontal hydrometeor mass transport reflects the weaker incident flow aloft and offshore flow at low levels at and

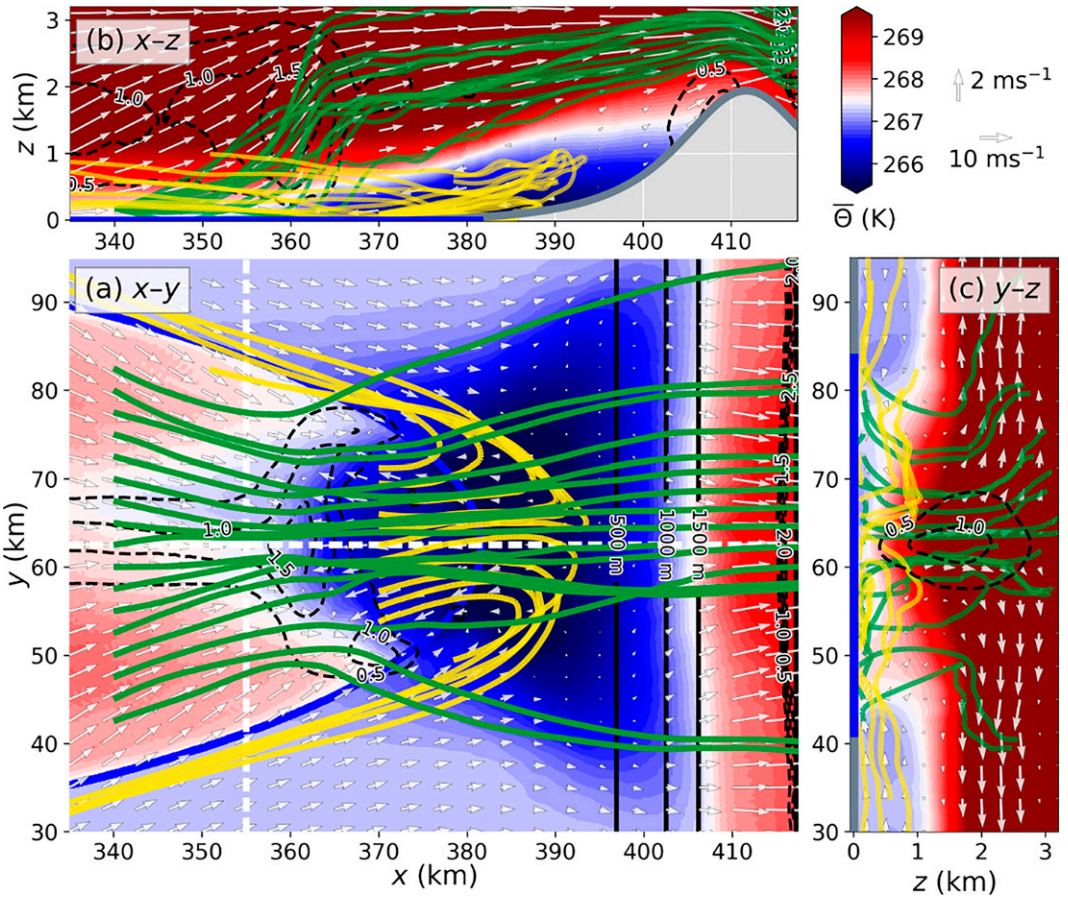

FIG. 6. BAND-2000R 4-h forward-calculated trajectories released at x = 340 km and z = 50 m (green) and 4-h backward-calculated trajectories released at x = 370 km and z = 50 m (yellow). (a) Plan-view analysis with 4-h time-mean lowest-level potential temperature ($\overline{\theta}$; K, scale at upper right), lowest-level (50-m) wind vectors (scale at upper right), and 1.5 km AGL vertical velocity (black dashed contours every 0.5 m s^{-1}). Thick blue line represents lake outline and solid black contours are elevation every 500 m from 500 to 1500 m. (b) As in (a), but for an x–z cross section through middle of the domain [illustrated by horizontal white dashed lien in (a)] and potential temperature, wind vectors, and vertical velocity are cross-section parallel. (c) As in (b), but for a y–z cross section at x = 355 km [illustrated by vertical white dashed line in (a)].

beneath the $\overline{q}$ maximum. Additionally, within the heavy precipitation region, the cloud base is depressed, resulting in a shallower subcloud layer and reduced sublimational losses (Fig. 5f). Farther inland, precipitation continues to decline over the ridge and ultimately features limited spillover in the downslope flow to the lee. Although hydrometeor mass growth increases over the upper windward slope where cross-barrier flow exists, there is little inland penetration of hydrometeor mass associated with the lake-effect system, which is largely depleted over the lake and lower mountain slope. Overall, these results indicate that the presence of the 2000-m ridge, in combination with surface heating over the lake, leads to the development of offshore flow that shifts the coastal baroclinic zone and precipitation maximum upstream.

c. *Lake–orographic circulations in BAND-2000R*

In this section, we present a trajectory analysis to illustrate the lake–orographic circulations in BAND-2000R. Following G21 (see their section 2d), trajectories were computed over the 4 h steady-state period from 90 s model output using open-source Python code described by Gowan (2019). To reduce the influence of turbulence, all model output is 20 × 20 × 2 point uniformly filtered.

We begin by analyzing the fate of overwater, lake-modified air as it approaches the coastal baroclinic zone, which we depict using forward-calculated air parcel trajectories starting at x = 340 km and 50 m AGL at the beginning of the steady-state period (i.e., hour 9) (Fig. 6; shown in green). Upstream of the coastal baroclinic zone, these trajectories migrate toward the midlake axis as they move downstream due to the thermally forced, cross-band secondary circulation (Fig. 6a). Near x = 365 km, the trajectories rise rapidly over the coastal baroclinic zone (Fig. 6b). Once lofted to z = 1–3 km, the parcels begin to diverge in the upper portion of the cross-band secondary circulation (Figs. 6a,c). Downstream of the coastal baroclinic zone, the trajectories slowly rise as they progress

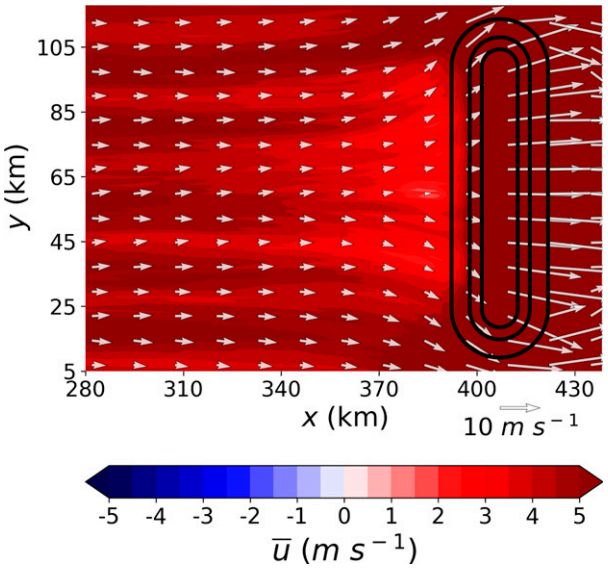

FIG. 7. Lowest-level (50-m), 4-h time-mean u wind (m s^{-1}, scale at bottom) and wind vectors (scale at bottom right) from a test simulation with a 2000-m ridge, but without a lake. Simulation run at 375-m grid spacing. Black elevation contours every 500 m from 500 to 1500 m.

downstream over the ridge, completely avoiding the low-level cold pool and the windward slope of the ridge (Fig. 6b).

We next examine the origins of the offshore flow that advects the cold pool and coastal baroclinic zone offshore using backward-calculated air parcel trajectories that end at x = 370 km and 50 m AGL at the end of the steady-state period (i.e., hour 13) (Fig. 6; shown in yellow). These trajectories originate within the continental air mass that flanks the lake and completely avoid lake modification as they move downstream (Figs. 6a,c). As they approach the ridge, they remain below 1 km AGL, enter the cold pool beneath the precipitation band, decelerate, reverse direction, and progress offshore (Figs. 6a,b).

Why do these dry, continental parcels fail to ascend the ridge? To address this question, we compute the nondimensional mountain height of the unsaturated, overland air, defined as

$$\hat{H} = \frac{N_d h_m}{U}, \tag{4}$$

where N_d is the dry Brunt–Väisälä frequency, h_m is the height of mountain barrier, and U is the component of wind normal to the barrier (e.g., Pierrehumbert and Wyman 1985; Smith 1988; Durran 1990). Using the mean N_d and U from the surface to 2 km AGL over all overland grid points along x = 355 km (dashed white line) in Fig. 6a, we compute $\hat{H}$ = 1.27. Theoretical and numerical modeling studies suggest that such values are sufficiently large to produce windward deceleration of the continental air mass and are near those needed produce flow stagnation (i.e., u = 0) given the horizontal aspect ratio (>4) of the 2000-m ridge (Bauer et al. 2000, see their Fig. 13). A test simulation without a lake, run at 375-m horizontal grid spacing, generated windward flow deceleration with very weak flow at z = 50 m near the windward base of the center of the ridge, but failed to produce flow reversal evident in BAND-2000R (Fig. 7). However, in BAND-2000R there is also localized heating produced by the oval lake. We hypothesize that the windward blocking in BAND-2000R sufficiently decelerates the large-scale flow to enable localized heating over the lake to not only produce a thermally forced circulation with converging flow from the flanking shorelines, but also offshore flow from the lee shoreline (e.g., yellow trajectories in Fig. 6a). While the former occurs in BAND-CTL and BAND-500P, along with weak flow in the downstream cold pool (Fig. 4), the latter develops only in BAND-2000R. Since there is no radiational cooling of the land surface in the simulation, it is not a contributor to the offshore flow, although it is possible that sublimational cooling does contribute (e.g., Hill 1978; Steiner et al. 2003). Although there is topography in BAND-500P, the lower height of the peak (500 m) leads to a smaller $\hat{H}$, which along with the smaller aspect ratio (~1), is less conducive to windward flow deceleration.

4. CELL orographic effects

a. Precipitation distribution

We now focus on the impact downstream terrain has on precipitation from broad-coverage, open-cell lake-effect systems (Fig. 8). Over the lake, the primary difference between CELL-500P and CELL-CTL is in the location and track of individual precipitation cells due to the random potential-temperature perturbations used to seed turbulence (Figs. 8a,b). This may contribute to differences in the location of accumulated precipitation bands prior to landfall, although upstream influences of terrain cannot be ruled out. Small contrasts in the spatial variations in wind and potential temperature also exist for this reason. Following landfall, precipitation over the peak in CELL-500P is stronger and more continuous than found over the same region in CELL-CTL, especially over the lee slope. Farther downstream of the peak, the precipitation rate is lower in CELL-500P than CELL-CTL. As a result, the total area-averaged precipitation only increases slightly from 0.13 mm h^{-1} in CELL-CTL to 0.14 mm h^{-1} in CELL-500P. However, the enhancement of cells interacting with the peak doubles the precipitation rate over the peak in CELL-500P compared to CELL-CTL, yielding an OR of 2.19 (Figs. 8b,d). Although the OR is somewhat dependent on the random development and track of cells, this doubling of precipitation is much greater than the 13% increase of precipitation produced over the peak in BAND-500P (Fig. 3d) and consistent with observed lake-effect events downstream of Lake Ontario, which exhibit greater precipitation enhancement over Tug Hill during non-banded periods than banded periods (Campbell et al. 2016; Veals et al. 2018).

In CELL-2000R, the 2000-m ridge significantly enhances open-cell lake-effect precipitation (Figs. 8c,e). Despite some deceleration over the windward slopes, the impinging flow moves over the ridge and precipitation rates increase dramatically, maximizing over and just downstream of the crest, before decreasing rapidly in the lee. This orographic enhancement roughly doubles the total area-averaged precipitation, yields a

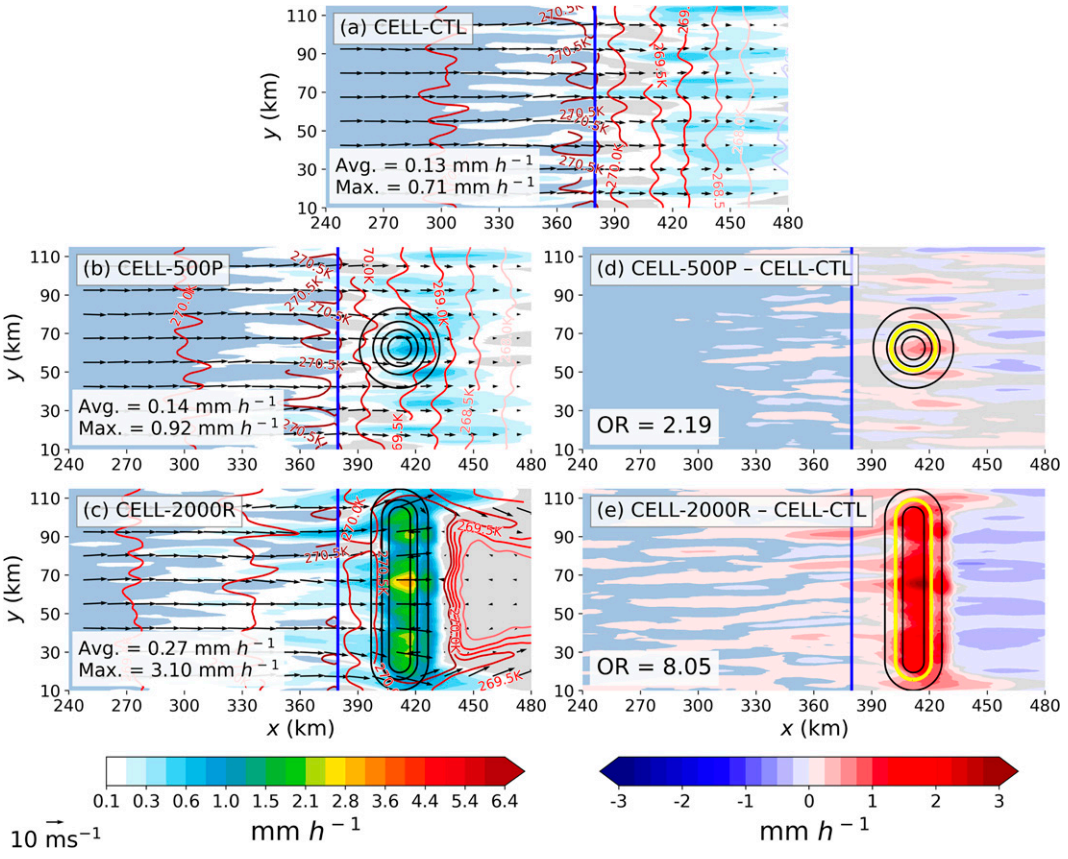

FIG. 8. As in Fig. 3, but for CELL simulations and (e) without OR_{band}.

maximum precipitation rate 4 times greater than in CELL-CTL, and results in an OR of 8.05, indicating a factor of 8 increase in precipitation over the ridge compared to a comparable area in CELL-CTL.

Close ups of the downstream coastline and terrain show a shift to stronger 1–1.5 km AGL vertically averaged vertical velocity in CELL-500P compared to CELL-CTL as the flow approaches and ascends the 500-m peak (Figs. 9a–d, note different color scales than Fig. 4). Over the lee slope, subsidence occurs. Precipitation associated with landfalling cells does not maximize over the windward slope, however, but over the lee slope, for reasons discussed in the next section.

In CELL-2000R, a spatially continuous zone of ascent begins just downstream of the coastline (Fig. 9f). The 1–1.5 km AGL vertically averaged vertical velocity increases abruptly to >1.0 m s^{-1} and precipitation rates increase over the windward slope (Figs. 9e,f). Over the crest, the precipitation rates maximize as the flow begins to descend in the lee wave. In contrast to BAND-2000R, which exhibits low-level stagnation and flow reversal due to the continental air flanking the oval lake interacting with the ridge, the flow throughout the domain in CELL-2000R experiences lake modification, leading to lower static stability and an $\hat{H} = 0.8$ (based on average values from x = 385–395 km, y = 52.5–72.5 km, and z = 0–2 km). The moist nondimensional mountain height $\hat{H}_m$, calculated using the moist Brunt–Väisälä frequency N_m rather than N_d, was 0.35. As a result, the flow moves over the ridge.

b. Vertical structure and hydrometeor tendencies

As in section 3b, we now use x–z cross sections to investigate how orography impacts the vertical structure and microphysical processes of the open-cell convection (Fig. 10). We present time-mean quantities but note that they include the influence of individual open cells that exhibit substantial variability, which we examine in greater depth in section 4c. Although we focus on the total hydrometeor mixing ratio ($\overline{q}$), the average open cell in all CELL simulations is composed primarily of $\overline{q}_s$ (~85%) and $\overline{q}_c$ (~13%).

Over water, the vertical structure and hydrometeor mass distribution of CELL-CTL and CELL-500P are relatively similar (Figs. 10a,b). Both simulations feature uniform winds and low $\overline{q}$, which maximizes at ~0.15 g kg^{-1} from z = 1.5–2 km. In CELL-CTL, there is a slight increase in $\overline{q}$ downstream of the coast followed by a decrease beyond x = 400 km where the zone of high $\overline{q}$ begins to arc gradually to the surface. In G21, we determined this structure reflects a convective-to-stratiform transition that begins at the coast with the convective vigor of individual cells declining and widespread, very weak ascent ($\overline{w} < 0.1$ m s^{-1}) developing as the warm, lake-modified air moves over the cool, inland air. The ascent generates the slight increase of $\overline{q}$ downstream of the coast, which arcs down to the

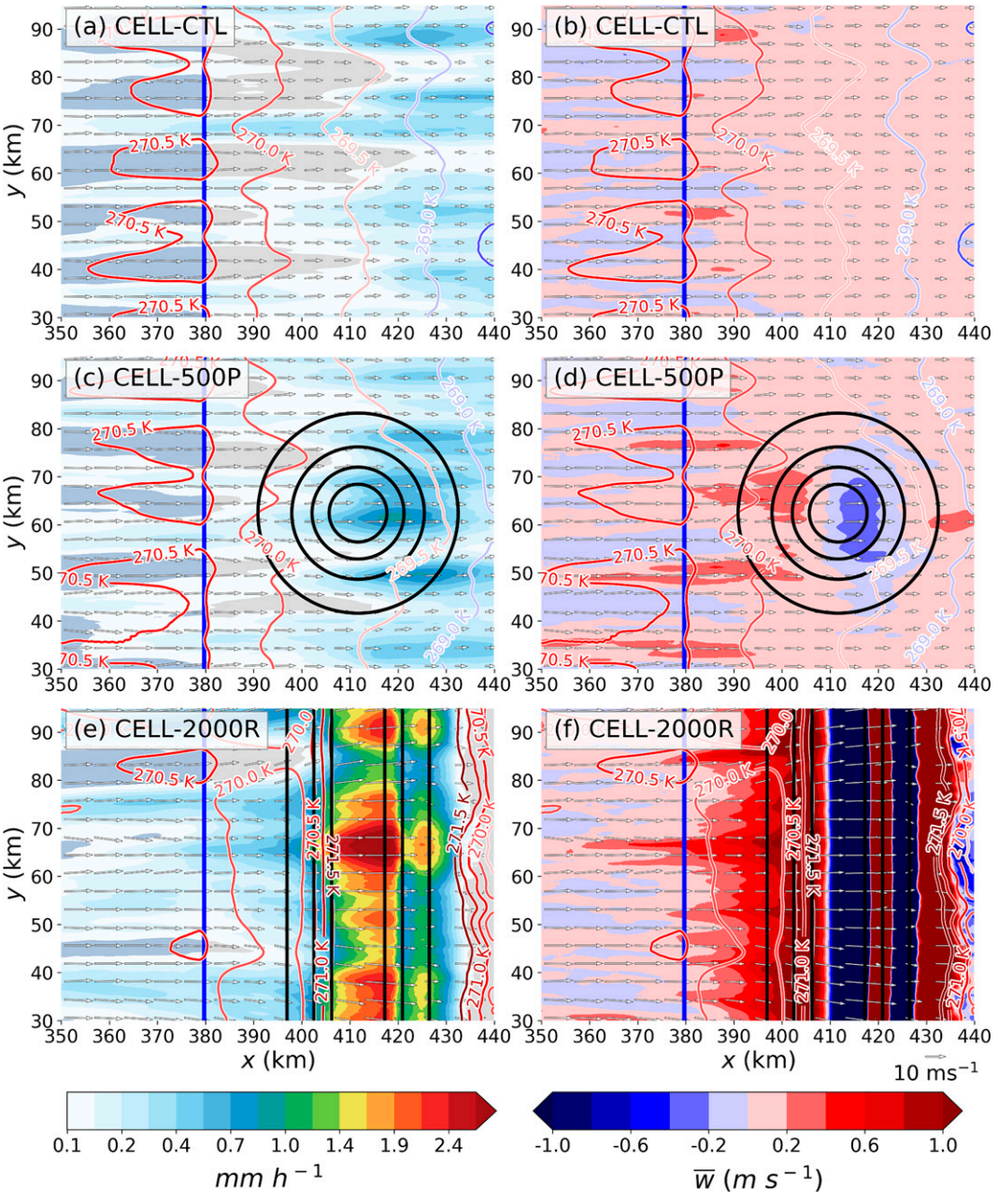

FIG. 9. As in Fig. 4, but for CELL simulations, slightly larger region, and different color scales for precipitation rate and $\overline{w}$.

surface near $x = 430$ km due to hydrometeor transport and fallout. In contrast, $\overline{q}$ downstream of the coast in CELL-500P increases as the flow ascends the windward slope of the peak, maximizes above the peak at ~0.25 g kg^{-1}, and then arcs downward, resulting in a surface maximum in $\overline{q}$ on the lee slope.

Further insights into the influence of the 500-m peak on the distribution of precipitation are provided by cross sections of $\overline{\text{qten}}$ and vertical velocity in CELL-CTL and CELL-500P (Figs. 10d,e). Whereas hydrometeor mass growth decreases with inland extent in CELL-CTL, CELL-500P exhibits a broad maximum in hydrometer mass growth associated with weak ascent ($\overline{w} < 0.1$ m s^{-1}) and reduced subcloud sublimation over the windward slope of the peak (Figs. 10d,e). The flow then descends the lee side of the peak resulting in a rapid decrease in growth and the formation of a deep layer (~2 km) of subcloud sublimation (Fig. 10e). The arcing maximum in $\overline{q}$ reflects an increase in hydrometeor mass growth over the windward slope and then subsequent hydrometeor mass transport and fallout to the surface of the lee slope (Figs. 10b,e). Overall, the moderate orographic precipitation enhancement (OR = 2.19; Fig. 8d) in CELL-500P is due to an orographic increase in hydrometeor mass growth, with transport and fallout

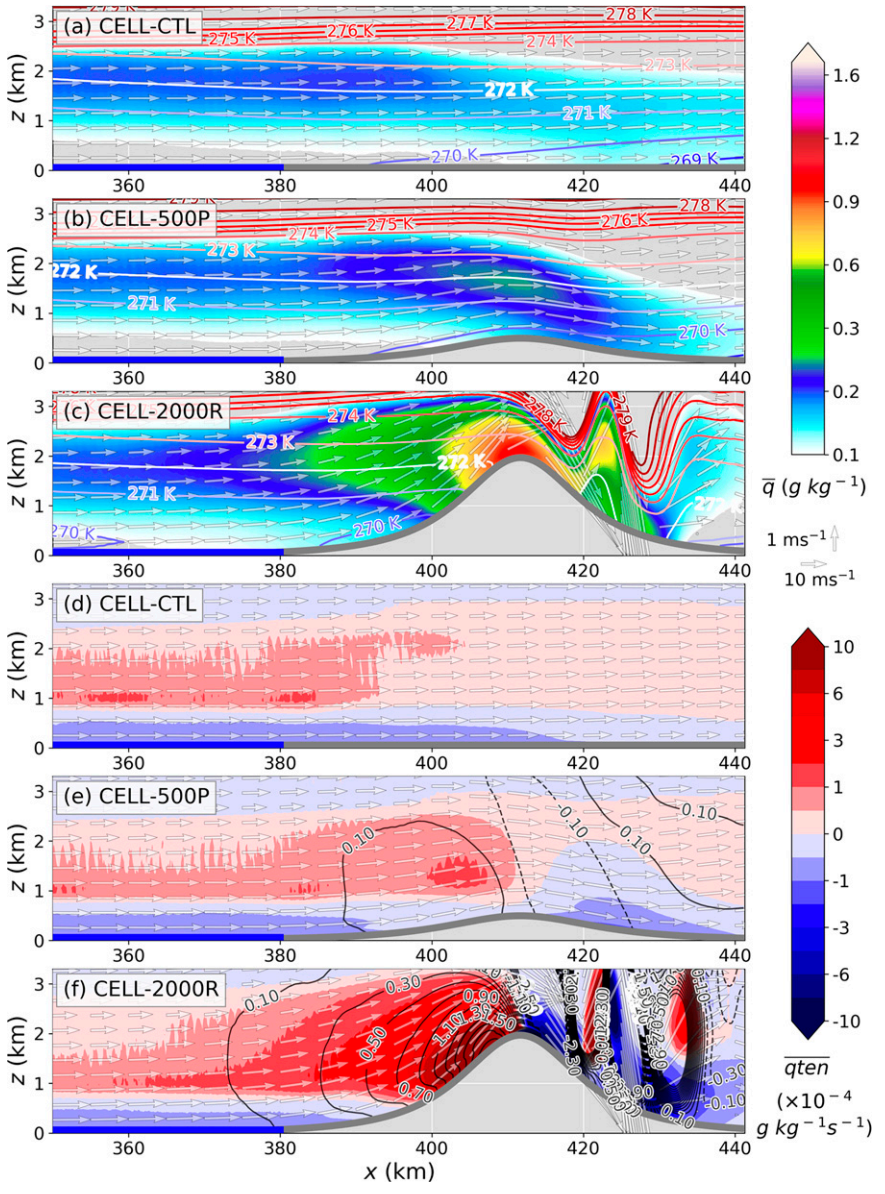

FIG. 10. As in Fig. 5, but for CELL simulations.

leading to enhanced precipitation rates near and downstream of the peak compared to CELL-CTL despite some hydrometeor mass loss due to sublimation in the descending, lee-side flow.

In CELL-2000R, $\overline{q}$ begins to increase near the coastline as the flow begins to ascend over the 2000-m ridge (Fig. 10c). The flow remains strong as it rises over the ridge and traverses the crest where $\overline{q}$ reaches a maximum of ~1.0 g kg^{-1} near the surface. The hydrometeor mass growth responsible for this $\overline{q}$ maximum occurs in the ascending flow over and upstream of the windward slope, especially where the flow is forced above cloud base (located at the transition from negative to positive $\overline{qten}$; Fig. 10f) and within about 500 m AGL of the mid and upper-windward slopes of the ridge. This area of intense hydrometeor growth is collocated with the ascent maximum, which reaches >2 m s^{-1} on the upper windward slope. Additionally, the top of the lake-effect system reaches above z = 3 km just upstream of the ridge, consistent with the upstream tilt of the mountain wave and higher than found in CELL-CTL and CELL-500P, as well as BAND-2000R. Downstream of the crest, hydrometeor transport and fallout results in moderate $\overline{q}$ (>0.3 g kg^{-1}) over the lee slope, but eventually a sharp cutoff in surface precipitation (see also Fig. 8c) as hydrometeor mass is carried upward in the hydraulic jump and strong sublimation occurs at low levels (Figs. 10c,f). This leads to a leeside "snow foot" resembling that observed in some orographic storms (e.g., Geerts et al. 2015). Overall, it is apparent that open-cell lake-effect experiences significant orographic enhancement as the mean flow ascends the ridge.

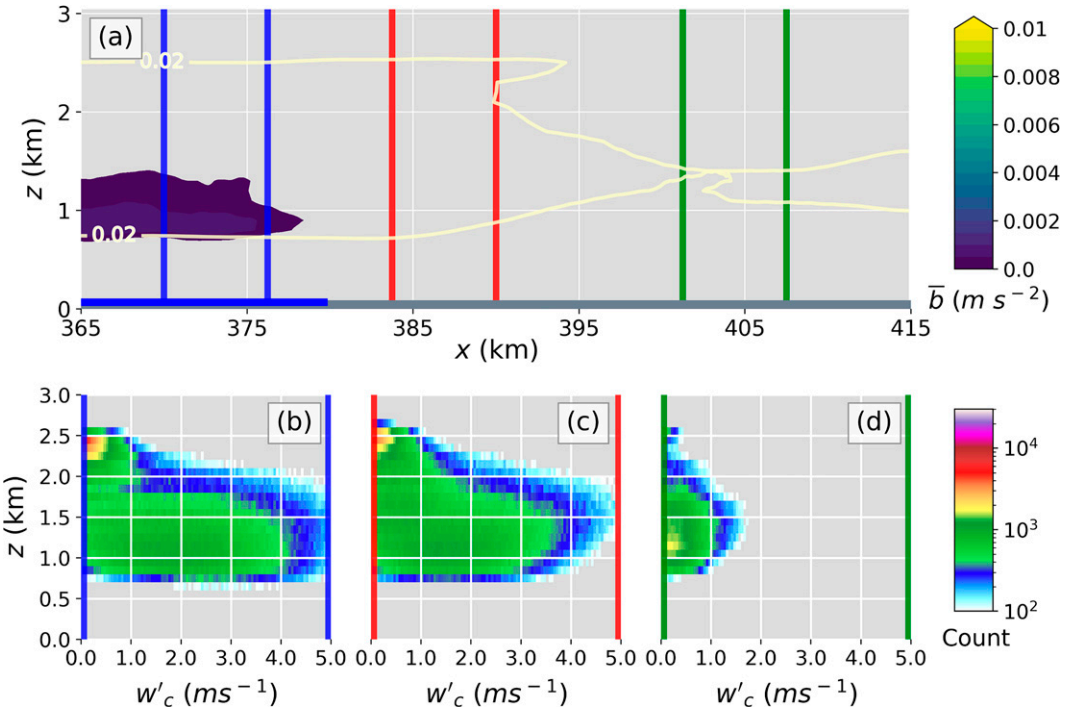

FIG. 11. (a) CELL-CTL x–z cross section of 4-h time-mean, 20-km y-averaged (centered over the middle of the domain's y axis) w'_c frequency (yellow to red contours every 0.04) and $\overline{b}$ (m s^{-2}, color filled following scale at middle right), each smoothed with a 30 × 2 point uniform filter. (b)–(d) 2D histograms of w'_c (total count) as a function of z and w'_c magnitude within the overwater, coastal, and inland regions bounded in (a) by blue, red, and green columns, respectively. Thick blue horizontal line in (a) represents the lake surface.

c. *Orographic influences on lake-effect convection*

We now examine how orography affects the characteristics of lake-effect convection. To establish a baseline, we first examine the characteristics of cloudy, convective updrafts, w'_c (hereafter convective updrafts), in CELL-CTL, which has no orography. Following Kirshbaum and Smith (2009), we define w'_c as a positive vertical velocity perturbation (i.e., $w' > 0$, where w' is the anomaly relative to the y-averaged and time averaged w) at a saturated (i.e., $q_c > 0$) grid point with a positive density potential temperature perturbation (i.e., $\theta'_\rho > 0$). $w'$and θ'_ρ are computed at each output time step relative to the 20-km y-average, 4-h time-mean, x–z cross section.

We present the frequency of occurrence of w'_c in 20-km-wide (y-direction) x–z cross section described above. Over water, convective updrafts are associated with open cells that are relatively sparse and occur 2%–6% of the time between z = 0.8–2.5 km (Fig. 11a, the lack of a 0.06 w'_c frequency contour indicates a maximum convective updraft frequency of less than 6%). Moving inland, this frequency begins to decline in the coastal plain (i.e., between the vertical red lines) and drops to ~2% in a shallow layer near $z \sim 1.4$ km farther inland (i.e., between the vertical green lines). These changes in the frequency, depth, and intensity of convective updrafts are further illustrated by 2D histograms of w'_c magnitude versus height over the water (i.e., between the vertical blue lines), coastal plain, and inland regions (Figs. 11b–d). Over water, this distribution is bimodal, with a high frequency of weak convective updrafts (≤0.5 m s^{-1}) near cloud top and a broad region of moderate convective updrafts (0.5–3 m s^{-1}) from z = 0.8–1.5 km (Fig. 11b). In some instances, convective updrafts over water reach 5 m s^{-1}. The distribution is generally similar in the coastal plain region, although there is a decrease in the frequency of stronger convective updrafts (i.e., >3 m s^{-1}) (Fig. 11c). In the inland region, however, there are no updrafts > 2 m s^{-1} and a decrease in updraft depth (Fig. 11d). Overall, these results are consistent with a decay in convective vigor and a convective-to-stratiform transition with inland extent.

Next, we examine the buoyancy of saturated (i.e., cloudy) updrafts relative to the unsaturated environment, $\overline{b}$. Following Kirshbaum and Smith [2009; their Eq. (2)], we define $\overline{b}$ as

$$\overline{b} = g\frac{\overline{\theta_{\rho c}} - \overline{\theta_{\rho 0}}}{\overline{\theta_{\rho 0}}} - g\frac{\overline{\theta_{\rho d}} - \overline{\theta_{\rho 0}}}{\overline{\theta_{\rho 0}}} = \frac{g}{\overline{\theta_{\rho 0}}}(\overline{\theta_{\rho c}} - \overline{\theta_{\rho d}}), \qquad (5)$$

where g is the acceleration of gravity, $\overline{\theta_{\rho c}}$ is the density potential temperature of grid points within the saturated updrafts (i.e., where $q_c > 0$ and $w' > 0$), $\overline{\theta_{\rho d}}$ is the density potential temperature of grid points within unsaturated downdrafts (i.e., where $q_c = 0$ and $w' > 0$), and $\overline{\theta_{\rho 0}}$ is the density potential temperature background state. All density potential temperatures are 20-km y-average, 4-h time mean in the x–z cross section. In CELL-CTL, clouds have weak buoyancy ($\overline{b} < 0.001$ m s^{-2}) over the lake near z = 1 km (Fig. 11a). Values near the coast and

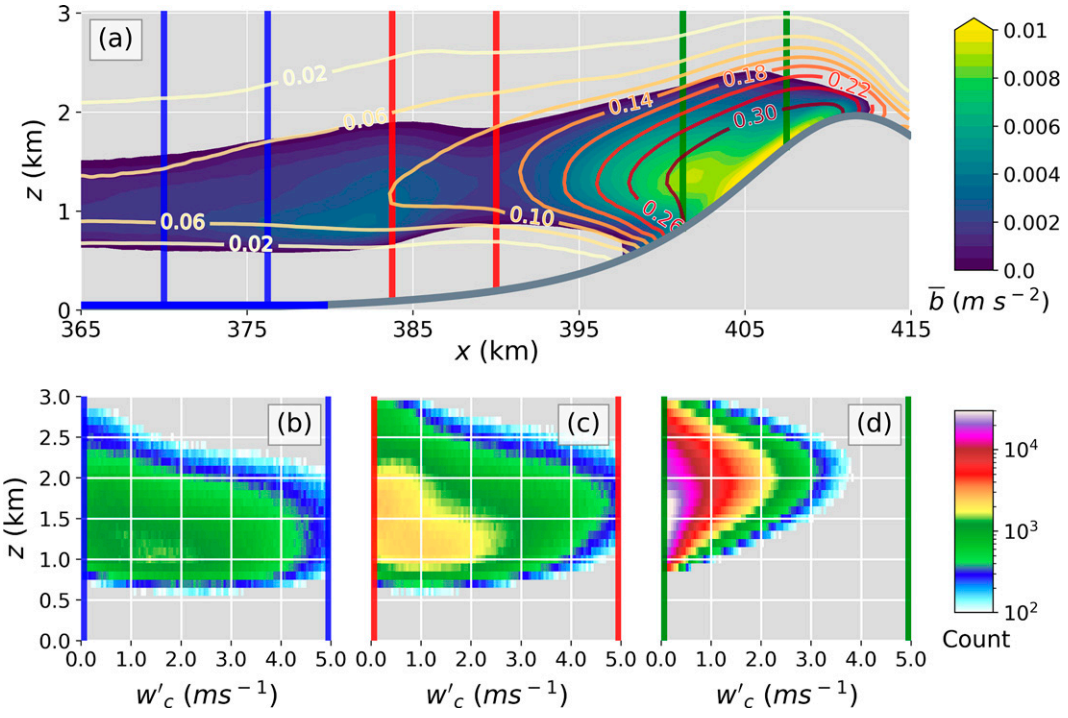

FIG. 12. As in Fig. 11, but for CELL-2000R.

inland are negative, indicating that the clouds are no longer buoyant, on average, as they penetrate inland.

In contrast, the presence of a 2000-m ridge results in dramatic changes in these convective measures in CELL-2000R (Fig. 12). Even over water, there is an increase in $\overline{b}$ and the frequency of convective updrafts compared to CELL-CTL, indicative of orographic influences extending upstream of the initial mountain slope (Fig. 12a). As the flow moves inland, orographic lifting of the inhomogeneous air in CELL-2000R generates buoyancy over the windward slope of the ridge as indicated by $\overline{b}$ increasing from <0.002 m s^{-2} above the base of the ridge (x = 390 km) to >0.008 m s^{-2} over the windward slope (x = 405 km). This may due to the differing lapse rates experienced by moist and dry parcels as they ascend the slope. Additionally, the frequency of cloudy updrafts roughly doubles over the same region from 0.1 to 0.14 above the base of the ridge to >0.3 over the windward slope. Although the 2D histograms of w'_c magnitude versus height are not substantially different compared to CELL-CTL over water (cf. Figs. 11b, 12b), they illustrate a strengthening and deepening of convective updrafts in the coastal zone of CELL-2000R with roughly 2 times the number of grid points with updrafts > 3 m s^{-1} and updrafts occasionally exceeding 3 km in height (cf. Figs. 11c, 12c). These updrafts shift upward and shallow over the windward slope of the ridge as the boundary layer top rises more slowly than the terrain, but updrafts > 2 m s^{-1} remain common (Fig. 12d). Overall, these results indicate that in contrast to the convective-to-stratiform transition that occurs in the absence of orography, bulk orographic ascent over the 2000-m ridge generates buoyancy and maintains or enhances convective vigor, leading to enhanced precipitation rates.

The orographic influences are less dramatic in CELL-500P but indicate some changes in convective characteristics compared to CELL-CTL (cf. Figs. 11, 13). For example, the frequency of convective updrafts in CELL-500P is higher at the coast and is ~3 times greater (~6% versus ~2%) over the windward slope of the peak (cf. Figs. 11a, 13a). The value of $\overline{b}$ is also greater near the coast. Comparison of 2D histograms reveals similar convective updraft statistics in CELL-500P and CELL-CTL over water (cf. Figs. 11b, 13b), but a slight increase in moderate to strong updraft frequency in the coastal region (cf. Figs. 11c, 13c) and a greater frequency of convective updrafts at all magnitudes up to ~2.5 m s^{-1} over the windward side of the peak (cf. Figs. 11d, 13d). Nevertheless, there are no updrafts > 2.5 m s^{-1} over the windward side of the peak, consistent with a decline the frequency of the strongest updrafts.

In summary, the presence of orography affects the characteristics of convective updrafts as lake-effect systems move inland. In the absence of terrain (i.e., CELL-CTL) a convective-to-stratiform transition occurs with a decline in buoyancy and convective vigor. The presence of a small peak (i.e., CELL-500P) yields an increase in the frequency of weak updrafts (i.e., <1 m s^{-1}), but there is still a decline in the frequency of the strongest updrafts. The presence of a large ridge (i.e., CELL-2000R), however, leads to orographic ascent that generates significant buoyancy and convective vigor with convective updrafts frequent and remaining strong, yielding significant orographic enhancement.

5. Conclusions

We have used idealized large-eddy simulations with simplified lake geometries to investigate the interaction of a

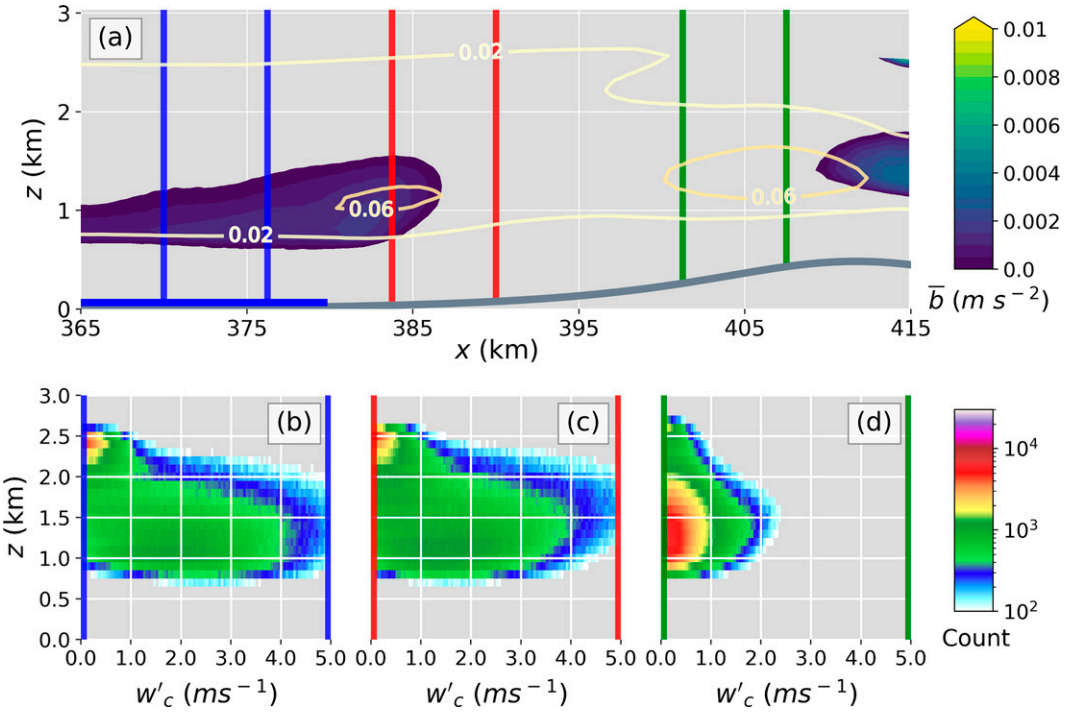

FIG. 13. As in Fig. 11, but for CELL-500P.

long-lake-axis-parallel (LLAP) band and broad-coverage, open-cell convection with a 500-m bell-shaped peak and a 2000-m ridge, focusing on the mechanisms responsible for differences in the distribution and orographic enhancement of lake-effect precipitation between the two modes. For the atmospheric conditions prescribed here, the LLAP band simulation without terrain (BAND-CTL) generates a coastal baroclinic zone over which ascent and hydrometeor mass within the landfalling LLAP band are maximized. Subsequent transport and fallout of hydrometeor mass leads to an inland precipitation maximum. The addition of a 500-m peak in the BAND-500P simulation does not substantially alter the structure of the LLAP band and produces only a 13% increase in precipitation over the peak. This increase is due to weak orographic ascent, which slightly increases hydrometeor mass growth, combined with reduced subcloud sublimation.

In contrast, the 2000-m ridge substantially alters the low-level flow and LLAP-band structure in the BAND-2000R simulation. In particular, the continental airstreams that flank the lake decelerate upstream of the ridge, merge beneath the LLAP band, and turn offshore. This low-level flow pattern appears to reflect the combined influence of windward flow deceleration and differential surface heating between the lake and land. The low-level offshore flow shifts the coastal baroclinic zone and associated ascent upstream, resulting in an offshore precipitation maximum. Ascent over the ridge is comparatively weak as the warm, lake-modified air ascends over the coastal baroclinic zone and then rises gradually as it progresses downstream across the ridge. As a result, precipitation decreases with inland extent, even over the ridge.

The simulations with an open lake that produce open-cell convection, however, exhibit much stronger orographic precipitation enhancement. The 500-m peak simulation (CELL-500P) generates increased hydrometeor mass growth above the windward slope which falls out over the lee slope due to subsequent hydrometeor transport and fallout. Although the hydrometeor mass falls through a relatively deep layer of sublimation as it descends over the lee slope, precipitation increases by a factor of 2.19 over the upper elevations of the peak compared to the same region in the simulation without topography (CELL-CTL). Enhancement in the 2000-m ridge simulation (CELL-2000R) is even greater with precipitation increasing by a factor of 8.05 over the upper elevations compared to the same region in the simulation without topography as the lake-modified flow downstream of the open lake readily ascends the ridge. In addition to the effects of bulk orographic ascent, the orographic enhancement over the ridge is also related to the strengthening of individual open cells as the cloudy, saturated updrafts gain buoyancy relative to the surrounding unsaturated dry air. In contrast, without topography, a convective-to-stratiform transition and loss of convective vigor occurs with inland extent. The addition of a 500-m peak does not prevent the decline of stronger updrafts as they move inland, although it does cause an increase in weaker (<1 m s^{-1}) updrafts.

Overall, these results illustrate some of the multifaceted ways that lake geometry, lake-effect mode, and the size and shape of downstream terrain may affect the distribution and intensity of precipitation (and snowfall) in landfalling lake-effect storms. The results of oval-lake simulations with a 500-m peak are broadly consistent with Campbell et al. (2016)

and Veals et al. (2018) who show that precipitation enhancement over the Tug Hill Plateau downstream of Lake Ontario is greater during broad coverage, non-banded periods than LLAP-band periods. The results of the 2000-m ridge simulations illustrate that the distribution of lake-effect precipitation is strongly dependent on whether or not the flow is blocked or unblocked, as one might expect from studies of orographic precipitation (e.g., Neiman et al. 2002; Bousquet and Smull 2003; Jiang 2003; Medina and Houze 2003; Rotunno and Houze 2007; Hughes et al. 2009) and as observed during lake-effect events in Japan where "satoyuki" storms with blocking produce heavy lowland precipitation upstream of the mountains and "yamayuki" storms in which the flow readily ascends the terrain produce heavy mountain precipitation (Magono et al. 1966; Ishihara et al. 1989; Kusunoki et al. 2004; Ohigashi et al. 2014; Veals et al. 2019, 2020; Steenburgh and Nakai 2020). The oval-lake simulation with a 2000-m ridge (BAND-2000R) also illustrates the potential for complex interactions between terrain- and lake-induced flows. Future work could explore such effects for a greater range of atmospheric conditions (e.g., wind speed and shear, boundary layer depth) and lake and terrain geometries, as well as the interaction of other lake-effect modes, such as longitudinal and transversal mode bands, with orography.

Acknowledgments. This material is based on work supported by the National Science Foundation under Grant AGS-1929602. Any opinions, findings, and conclusions or recommendations expressed in this material are those of the authors and do not necessarily reflect the views of the National Science Foundation. John Horel, Court Strong, and David Gagne provided comments and input that significantly improved the manuscript. We thank George Bryan and NCAR for providing the CM1 code and acknowledge the use of computer resources (doi:10.5065/D6RX99HX) at the NCAR–Wyoming Supercomputing Center provided by the National Science Foundation and State of Wyoming and supported by NCAR's Computational and Information Systems Laboratory. We also thank the University of Utah Center for High Performance Computing and Jeremy Gibbs for computer resources and assistance.

Data availability statement. The total volume of CM1 output from the simulations used for this study is 18 TB. Contact the corresponding author for access to the CM1 model output, which is stored on servers at the University of Utah Center for High Performance Computing.

REFERENCES

Alcott, T. I., and W. J. Steenburgh, 2013: Orographic influences on a Great Salt Lake–effect snowstorm. *Mon. Wea. Rev.*, **141**, 2432–2450, https://doi.org/10.1175/MWR-D-12-00328.1.

Andersson, T., and N. Gustafsson, 1994: Coast of departure and coast of arrival: Two important concepts for the formation and structure of convective snowbands over seas and lakes. *Mon. Wea. Rev.*, **122**, 1036–1049, https://doi.org/10.1175/1520-0493(1994)122<1036:CODACO>2.0.CO;2.

Atkinson, B., and J. Zhang, 1996: Mesoscale shallow convection in the atmosphere. *Rev. Geophys.*, **34**, 403–431, https://doi.org/10.1029/96RG02623.

Atlas, D., S.-H. Chou, and W. P. Byerly, 1983: The influence of coastal shape on winter mesoscale air–sea interaction. *Mon. Wea. Rev.*, **111**, 245–252, https://doi.org/10.1175/1520-0493(1983)111<0245:TIOCSO>2.0.CO;2.

Bauer, M. H., G. J. Mayr, I. Vergeiner, and H. Pichler, 2000: Strongly nonlinear flow over and around a three-dimensional mountain as a function of the horizontal aspect ratio. *J. Atmos. Sci.*, **57**, 3971–3991, https://doi.org/10.1175/1520-0469(2001)058<3971:SNFOAA>2.0.CO;2.

Bergmaier, P. T., B. Geerts, L. S. Campbell, and W. J. Steenburgh, 2017: The OWLeS IOP2b lake-effect snowstorm: Dynamics of the secondary circulation. *Mon. Wea. Rev.*, **145**, 2437–2459, https://doi.org/10.1175/MWR-D-16-0462.1.

Bousquet, O., and B. F. Smull, 2003: Observations and impacts of upstream orographic blocking during a widespread orographic precipitation event. *Quart. J. Roy. Meteor. Soc.*, **129**, 391–409, https://doi.org/10.1256/qj.02.49.

Braham, R. R., 1983: The Midwest snow storm of 8–11 December 1977. *Mon. Wea. Rev.*, **111**, 253–272, https://doi.org/10.1175/1520-0493(1983)111<0253:TMSSOD>2.0.CO;2.

——, 1986: Cloud and motion fields in open-cell convection over Lake Michigan. Preprints, *Joint Session—23rd Conf. on Radar Meteorology and Conf. on Cloud Physics*, Snowmass, CO, Amer. Meteor. Soc., JP202–JP205.

——, and R. D. Kelly, 1982: Lake-effect snow storms on Lake Michigan, USA. *Cloud Dynamics*, E. M. Agee and T. Asai, Eds., D. Reidel, 87–101.

Bryan, G. H., and J. M. Fritsch, 2002: A benchmark simulation for moist nonhydrostatic numerical models. *Mon. Wea. Rev.*, **130**, 2917–2928, https://doi.org/10.1175/1520-0493(2002)130<2917:ABSFMN>2.0.CO;2.

Burt, C. A., 2007: *Extreme Weather.* 2nd ed. W. W. Norton and Company, 320 pp.

Campbell, L. S., and W. J. Steenburgh, 2017: The OWLeS IOP2b lake-effect snowstorm: Mechanisms contributing to the Tug Hill precipitation maximum. *Mon. Wea. Rev.*, **145**, 2461–2478, https://doi.org/10.1175/MWR-D-16-0461.1.

——, ——, P. G. Veals, T. W. Letcher, and J. R. Minder, 2016: Lake-effect mode and precipitation enhancement over the Tug Hill Plateau during OWLeS IOP2b. *Mon. Wea. Rev.*, **144**, 1729–1748, https://doi.org/10.1175/MWR-D-15-0412.1.

Dörnbrack, A., J. D. Doyle, T. P. Lane, R. D. Sharman, and P. K. Smolarkiewicz, 2005: On physical realizability and uncertainty of numerical solutions. *Atmos. Sci. Lett.*, **6**, 118–122, https://doi.org/10.1002/asl.100.

Dudhia, J., 1996: A multi-layer soil temperature model for MM5. Preprints, *Sixth PSU/NCAR Mesoscale Model Users' Workshop*, Boulder, CO, PSU and NCAR, 49–50.

Durran, D. R., 1990: Mountain waves and downslope winds. *Atmospheric Processes over Complex Terrain, Meteor. Monogr.*, No. 45, Amer. Meteor. Soc., 59–81.

Geerts, B., Y. Yang, R. Rasmussen, S. Haimov, and B. Pokharel, 2015: Snow growth and transport patterns in orographic storms as estimated from airborne vertical-plane dual-Doppler radar data. *Mon. Wea. Rev.*, **143**, 644–665, https://doi.org/10.1175/MWR-D-14-00199.1.

Gowan, T. M., 2019: Trajectories. GitHub, accessed 9 October 2019, https://github.com/tomgowan/trajectories.

——, W. J. Steenburgh, and J. Minder, 2021: Downstream evolution and coastal-to inland transition of landfalling lake-effect

systems. *Mon. Wea. Rev.*, **149**, 1023–1040, https://doi.org/10.1175/MWR-D-20-0253.1.

Great Lakes Environmental Research Laboratory, 2021: Great Lakes statistics. NOAA, accessed 15 February 2015, https://coastwatch.glerl.noaa.gov/statistic/.

Hartnett, J. J., J. M. Collins, M. A. Baxter, and D. P. Chambers, 2014: Spatiotemporal snowfall trends in central New York. *J. Appl. Meteor. Climatol.*, **53**, 2685–2697, https://doi.org/10.1175/JAMC-D-14-0084.1.

Hill, G. E., 1978: Observations of precipitation-forced circulations in winter orographic storms. *J. Atmos. Sci.*, **35**, 1463–1472, https://doi.org/10.1175/1520-0469(1978)035<1463:OOPFCI>2.0.CO;2.

Hjelmfelt, M. R., 1990: Numerical study of the influence of environmental conditions on lake-effect snowstorms over Lake Michigan. *Mon. Wea. Rev.*, **118**, 138–150, https://doi.org/10.1175/1520-0493(1990)118<0138:NSOTIO>2.0.CO;2.

Houze, R., 2012: Orographic effects on precipitating clouds. *Rev. Geophys.*, **50**, RG1001, https://doi.org/10.1029/2011RG000365.

Hughes, M., A. Hall, and R. G. Fovell, 2009: Blocking in areas of complex topography, and its influence on rainfall distribution. *J. Atmos. Sci.*, **66**, 508–518, https://doi.org/10.1175/2008JAS2689.1.

Ishihara, M., H. Sakakibara, and Z. Yanagisawa, 1989: Doppler radar analysis of the structure of mesoscale snow bands developed between the winter monsoon and the land breeze. *J. Meteor. Soc. Japan*, **67**, 503–520, https://doi.org/10.2151/jmsj1965.67.4_503.

Jiang, Q., 2003: Moist dynamics and orographic precipitation. *Tellus*, **55A**, 301–316, https://doi.org/10.3402/tellusa.v55i4.14577.

Jiménez, P. A., J. Dudhia, J. F. González-Rouco, J. Navarro, J. P. Montávez, and E. García-Bustamante, 2012: A revised scheme for the WRF surface layer formulation. *Mon. Wea. Rev.*, **140**, 898–918, https://doi.org/10.1175/MWR-D-11-00056.1.

Kawamoto, T. S., S. Miyazawa, and K. Fuj, 1963: Heavy snowfalls caused by the Hokuriku Front. *Kisho Kenyo Noto.*, **14**, 56–70.

Kindap, T., 2010: A severe sea-effect snow episode over the city of Istanbul. *Nat. Hazards*, **54**, 707–723, https://doi.org/10.1007/s11069-009-9496-7.

Kirshbaum, D. J., and R. B. Smith, 2009: Orographic precipitation in the tropics: Large-eddy simulations and theory. *J. Atmos. Sci.*, **66**, 2559–2578, https://doi.org/10.1175/2009JAS2990.1.

Kristovich, D. A. R., and Coauthors, 2017: The Ontario winter lake-effect systems field campaign: Scientific and educational adventures to further our knowledge and prediction of lake-effect storms. *Bull. Amer. Meteor. Soc.*, **98**, 315–332, https://doi.org/10.1175/BAMS-D-15-00034.1.

Kusunoki, K., M. Murakami, M. Hoshimoto, N. Orikasa, Y. Yamada, H. Mizuno, K. Hamazu, and H. Watanabe, 2004: The characteristics and evolution of orographic snow clouds under weak cold advection. *Mon. Wea. Rev.*, **132**, 174–191, https://doi.org/10.1175/1520-0493(2004)132<0174:TCAEOO>2.0.CO;2.

Lackmann, G., 2011: *Midlatitude Synoptic Meteorology: Dynamics, Analysis, and Forecasting.* Amer. Meteor. Soc., 360 pp.

Laird, N. F., J. E. Walsh, and D. A. R. Kristovich, 2003a: Model simulations examining the relationship of lake-effect morphology to lake shape, wind direction, and wind speed. *Mon. Wea. Rev.*, **131**, 2102–2111, https://doi.org/10.1175/1520-0493(2003)131<2102:MSETRO>2.0.CO;2.

——, D. A. R. Kristovich, and J. E. Walsh, 2003b: Idealized model simulations examining the mesoscale structure of winter lake-effect circulations. *Mon. Wea. Rev.*, **131**, 206–221, https://doi.org/10.1175/1520-0493(2003)131<0206:IMSETM>2.0.CO;2.

Magono, C., K. Kikuchi, T. Kimura, S. Tazawa, and T. Kasai, 1966: A study on the snowfall in the winter monsoon season in Hokkaido with special reference to low land snowfall. *J. Fac. Sci. Hokkaido Univ. Ser.*, **7**, 287–308.

Markowski, P., and Y. Richardson, 2010: *Mesoscale Meteorology in Midlatitudes.* Wiley-Blackwell, 407 pp.

——, and G. H. Bryan, 2016: LES of laminar flow in the PBL: A potential problem for convective storm simulations. *Mon. Wea. Rev.*, **144**, 1841–1850, https://doi.org/10.1175/MWR-D-15-0439.1.

Mazon, J., S. Niemela, D. Pino, H. Savijärvi, and T. Vihma, 2015: Snow bands over the Gulf of Finland in wintertime. *Tellus*, **67A**, 25102, https://doi.org/10.3402/tellusa.v67.25102.

Medina, S., and R. A. Houze Jr., 2003: Air motions and precipitation growth in Alpine storms. *Quart. J. Roy. Meteor. Soc.*, **129**, 345–371, https://doi.org/10.1256/qj.02.13.

Minder, J. R., T. W. Letcher, L. S. Campbell, P. G. Veals, and W. J. Steenburgh, 2015: The evolution of lake-effect convection during landfall and orographic uplift as observed by profiling radars. *Mon. Wea. Rev.*, **143**, 4422–4442, https://doi.org/10.1175/MWR-D-15-0117.1.

Murakami, M., T. Clark, and W. Hall, 1994: Numerical simulations of convective snow clouds over the Sea of Japan: Two-dimensional simulations of mixed layer development and convective snow cloud formation. *J. Meteor. Soc. Japan*, **72**, 43–62, https://doi.org/10.2151/jmsj1965.72.1_43.

Nagata, M., 1987: On the formation of a convergent cloud band over the Japan Sea in winter; a prediction experiment. *J. Meteor. Soc. Japan*, **65**, 871–883, https://doi.org/10.2151/jmsj1965.65.6_871.

——, 1991: Further numerical study on the formation of the convergent cloud band over the Japan Sea in winter. *J. Meteor. Soc. Japan*, **69**, 419–428, https://doi.org/10.2151/jmsj1965.69.3_419.

——, M. Ikawa, S. Yoshizumi, and T. Yoshida, 1986: On the formation of a convergent cloud band over the Japan Sea in winter; numerical experiments. *J. Meteor. Soc. Japan*, **64**, 841–855, https://doi.org/10.2151/jmsj1965.64.6_841.

Nakai, S., M. Maki, and T. Yagi, 1990: Doppler radar observation of orographic modification of snow clouds—A case of enhanced snowfall. Report of the National Research Center for Disaster Prevention, Rep. 45, 16 pp.

——, K. Iwanami, R. Misumi, S.-G. Park, and T. Kobayashi, 2005: A classification of snow clouds by Doppler radar observations at Nagaoka, Japan. *SOLA*, **1**, 161–164, https://doi.org/10.2151/sola.2005-042.

Neiman, P. J., F. M. Ralph, A. B. White, D. E. Kingsmill, and P. O. G. Persson, 2002: The statistical relationship between upslope flow and rainfall in California's Coastal Mountains: Observations during CALJET. *Mon. Wea. Rev.*, **130**, 1468–1492, https://doi.org/10.1175/1520-0493(2002)130<1468:TSRBUF>2.0.CO;2.

Nicholls, F. J., and R. Toumi, 2014: On the lake effects of the Caspian Sea. *Quart. J. Roy. Meteor. Soc.*, **140**, 1399–1408, https://doi.org/10.1002/qj.2222.

Niziol, T. A., 1987: Operational forecasting of lake effect snowfalls in western and central New York. *Wea. Forecasting*, **2**, 310–321, https://doi.org/10.1175/1520-0434(1987)002<0310:OFOLES>2.0.CO;2.

——, W. R. Snyder, and J. S. Waldstreicher, 1995: Winter weather forecasting throughout the eastern United States. Part IV:

Lake effect snow. *Wea. Forecasting*, **10**, 61–77, https://doi.org/10.1175/1520-0434(1995)010<0061:WWFTTE>2.0.CO;2.

Norris, J., G. Vaugh, and D. M. Schultz, 2013: Snowbands over the English Channel and Irish Sea during cold-air outbreaks. *Quart. J. Roy. Meteor. Soc.*, **139**, 1747–1761, https://doi.org/10.1002/qj.2079.

Ohigashi, T., and K. Tsuboki, 2007: Shift and intensification processes of the Japan-Sea polar-airmass convergence zone associated with the passage of a mid-tropospheric cold core. *J. Meteor. Soc. Japan*, **85**, 633–662, https://doi.org/10.2151/jmsj.85.633.

——, ——, Y. Schusse, and H. Uyeda, 2014: An intensification process of a winter broad cloud band on a flank of the mountain region along the Japan-Sea coast. *J. Meteor. Soc. Japan*, **92**, 71–93, https://doi.org/10.2151/jmsj.2014-105.

Peace, R., Jr., and R. Sykes Jr., 1966: Mesoscale study of a lake effect snow storm. *Mon. Wea. Rev.*, **94**, 495–507, https://doi.org/10.1175/1520-0493(1966)094<0495:MSOALE>2.3.CO;2.

Pierrehumbert, R. T., and B. Wyman, 1985: Upstream effects of mesoscale mountains. *J. Atmos. Sci.*, **42**, 977–1003, https://doi.org/10.1175/1520-0469(1985)042<0977:UEOMM>2.0.CO;2.

Reinking, R. F., and Coauthors, 1993: The Lake Ontario Winter Storms (LOWS) project. *Bull. Amer. Meteor. Soc.*, **74**, 1828–1850, https://doi.org/10.1175/1520-0477-74-10-1828.

Roe, G. H., 2005: Orographic precipitation. *Annu. Rev. Earth Planet. Sci.*, **33**, 645–671, https://doi.org/10.1146/annurev.earth.33.092203.122541.

Rotunno, R., and R. A. Houze Jr., 2007: Lessons on orographic precipitation from the Mesoscale Alpine Programme. *Quart. J. Roy. Meteor. Soc.*, **133**, 811–830, https://doi.org/10.1002/qj.67.

Saito, K., M. Murakami, T. Matsuo, and H. Mizuno, 1996: Sensitivity experiments on the orographic snowfall over the mountainous region of northern Japan. *J. Meteor. Soc. Japan*, **74**, 797–813, https://doi.org/10.2151/jmsj1965.74.6_797.

Smagorinsky, J., 1963: General circulation experiments with the primitive equations. Part I: The basic experiments. *Mon. Wea. Rev.*, **91**, 99–164, https://doi.org/10.1175/1520-0493(1963)091<0099:GCEWTP>2.3.CO;2.

Smith, R. B., 1988: Linear theory of stratified flow past an isolated mountain in isosteric coordinates. *J. Atmos. Sci.*, **45**, 3889–3896, https://doi.org/10.1175/1520-0469(1988)045<3889:LTOSFP>2.0.CO;2.

——, 2006: Progress on the theory of orographic precipitation. *Special Paper 398: Tectonics, Climate, and Landscape Evolution*, Geological Society of America, Boulder, CO, 16 pp.

Steenburgh, W. J., and L. S. Campbell, 2017: The OWLeS IOP2b lake-effect snowstorm: Shoreline geometry and the mesoscale forcing of precipitation. *Mon. Wea. Rev.*, **145**, 2421–2436, https://doi.org/10.1175/MWR-D-16-0460.1.

——, and S. Nakai, 2020: Perspectives on sea- and lake-effect precipitation from Japan's "Gosetsu Chitai." *Bull. Amer. Meteor. Soc.*, **101**, E58–E72, https://doi.org/10.1175/BAMS-D-18-0335.1.

——, S. F. Halvorson, and D. J. Onton, 2000: Climatology of lake-effect snowstorms of the Great Salt Lake. *Mon. Wea. Rev.*, **128**, 709–727, https://doi.org/10.1175/1520-0493(2000)128<0709:COLESO>2.0.CO;2.

Steiger, S. M., and Coauthors, 2013: Circulations, bounded weak echo regions, and horizontal vortices observed within long-lake-axis-parallel–lake-effect storms by the Doppler on Wheels. *Mon. Wea. Rev.*, **141**, 2821–2840, https://doi.org/10.1175/MWR-D-12-00226.1.

Steiner, M., O. Bousquet, R. A. Houze, B. F. Smull, and M. Mancini, 2003: Airflow within major Alpine river valleys under heavy rainfall. *Quart. J. Roy. Meteor. Soc.*, **129**, 411–431, https://doi.org/10.1256/qj.02.08.

Thompson, G., P. R. Field, R. M. Rasmussen, and W. D. Hall, 2008: Explicit forecasts of winter precipitation using an improved bulk microphysics scheme. Part II: Implementation of a new snow parameterization. *Mon. Wea. Rev.*, **136**, 5095–5115, https://doi.org/10.1175/2008MWR2387.1.

Tripoli, G. J., 2005: Numerical study of the 10 January 1998 lake-effect bands observed during Lake-ICE. *J. Atmos. Sci.*, **62**, 3232–3249, https://doi.org/10.1175/JAS3462.1.

Tsuchiya, K., and T. Fujita, 1967: A satellite meteorological study of evaporation and cloud formation over the western Pacific under the influence of the winter monsoon. *J. Meteor. Soc. Japan*, **45**, 232–250, https://doi.org/10.2151/jmsj1965.45.3_232.

Umek, L., and A. Gohm, 2016: Lake and orographic effects on a snowstorm at Lake Constance. *Mon. Wea. Rev.*, **144**, 4687–4707, https://doi.org/10.1175/MWR-D-16-0032.1.

Veals, P. G., and W. J. Steenburgh, 2015: Climatological characteristics and orographic enhancement of lake-effect precipitation east of Lake Ontario and over the Tug Hill Plateau. *Mon. Wea. Rev.*, **143**, 3591–3609, https://doi.org/10.1175/MWR-D-15-0009.1.

——, ——, and L. S. Campbell, 2018: Factors affecting the inland and orographic enhancement of lake-effect precipitation over the Tug Hill Plateau. *Mon. Wea. Rev.*, **146**, 1745–1762, https://doi.org/10.1175/MWR-D-17-0385.1.

——, ——, S. Nakai, and S. Yamaguchi, 2019: Factors affecting the inland and orographic enhancement of sea-effect snowfall in the Hokuriku region of Japan. *Mon. Wea. Rev.*, **147**, 3121–3143, https://doi.org/10.1175/MWR-D-19-0007.1.

——, ——, ——, and ——, 2020: Intrastorm variability of the inland and orographic enhancement of a sea-effect snowstorm in the Hokuriku region of Japan. *Mon. Wea. Rev.*, **148**, 2527–2548, https://doi.org/10.1175/MWR-D-19-0390.1.

West, T. K., W. J. Steenburgh, and G. G. Mace, 2019: Characteristics of sea-effect clouds and precipitation over the Sea of Japan region as observed by A-Train satellites. *J. Geophys. Res. Atmos.*, **124**, 1322–1335, https://doi.org/10.1029/2018JD029586.

Yamaguchi, S., O. Abe, S. Nakai, and A. Sato, 2011: Recent fluctuations of meteorological and snow conditions in Japanese mountains. *Ann. Glaciol.*, **52**, 209–215, https://doi.org/10.3189/172756411797252266.